VILNIUS UNIVERSITY
FACULTY OF CHEMISTRY AND GEOSCIENCES
INSTITUTE OF CHEMISTRY
DEPARTMENT OF INORGANIC CHEMISTRY

Dovydas Karoblis
Degree programme Chemistry
Master thesis

SYNTHESIS AND CHARACTERIZATION OF BiMnO₃ CONTAINING SOLID SOLUTIONS

Scientific adviser
Prof. Habil. Dr. Aivaras Kareiva

_____
(permission to defend, date, signature)
Scientific consultant
Dr. Aleksej Žarkov

Date of submission _____
Registration No. _____

Vilnius 2020

CONTENT

LIST OF ABBREVIATIONS

BMO – Bismuth manganite (BiMnO$_3$)
BTO – Barium titanate (BaTiO$_3$)
DSC – Differential scanning calorimetry
DTG – Differential thermogravimetry
FT-IR – Fourier transform infrared spectroscopy
SEM – Scanning electron microscopy
STO – Strontium titanate (SrTiO$_3$)
TG – Thermogravimetry
XRD – X-ray diffraction

INTRODUCTION

Calcium titanium oxide ($CaTiO_3$) was the first discovered compound with the structure, which is now known as perovskite [1]. The formula of these materials is ABX_3, where A and B are cations with A size larger than that B and X is the anion. Perovskites generally can be classified in to two types: chalcogenides (where X is oxygen) and halide perovskites (where X is halide) [2]. Due to high variation of different elements in A and B sites, both perovskite classes can offer great amount of various properties, including magnetism, ferroelectricity, piezoelectricity, pyroelectricity, dielectricity, superconductivity, catalytic etc [3–6]. As a result of great variety of properties, these materials can be applied in different devices such as solid oxide fuel cells, multifunctional memory devices, gas sensors and much more [7–11].

$BiMnO_3$ perovskite, which exhibits coexistence of ferromagnetic and ferroelectric properties, is regarded as one of the most prominent multiferroic materials [12]. However, it cannot be synthesized under ambient conditions and usually it is prepared by high-pressure and high-temperature synthesis [13]. On the other hand, solid solutions containing a substantial amount of $BiMnO_3$ could lead to easier synthesis conditions and demonstration of $BiMnO_3$-like properties [14].

In the present work, few functional materials were chosen for the preparation of solid solutions with $BiMnO_3$. For this purpose, oxide materials, which can be easily synthesized using different synthetic approaches, were selected. For example, considering–$LaMnO_3$– both Bi^{3+} and La^{3+} are similar in ionic size and valence and it was observed that, the substitution of Bi^{3+} by La^{3+} ions can lead to smaller distortions and lower synthesis temperatures during the preparation of Bi-rich $Bi_xLa_{1-x}MnO_3$ solid solutions [15]. Furthermore, $BaTiO_3$ and $SrTiO_3$ materials can be easily prepared by different techniques and partial substitution of one or both cations can cause changes in physical properties [16,17].

The main aim of this work was to prepare different $BiMnO_3$-containing perovskite-type solid solutions by simple and cost-effective techniques including aqueous sol-gel and sol-gel combustion methods investigating the effect of chemical composition on the characteristics of the end products. The additional aim was to determine maximal percentage of $BiMnO_3$ in solid solutions depending on the host material. The following tasks were set up in order to achieve these objectives:

- Synthesis and characterization of $LaMnO_3$-$BiMnO_3$ solid solutions.
- Synthesis and characterization of $BaTiO_3$-$BiMnO_3$ solid solutions.
- Synthesis and characterization of $SrTiO_3$-$BiMnO_3$ solid solutions.
- Investigation of the maximal amount of $BiMnO_3$ in $LaMnO_3$-$BiMnO_3$, $BaTiO_3$-$BiMnO_3$, $SrTiO_3$-$BiMnO_3$ solid solutions.

1. LITERATURE REVIEW

1.1 Perovskites

Perovskites are the large family of compounds that have crystal structure related to the mineral perovskite $CaTiO_3$. General formula for perovskites is ABX_3 where, A and B are two cations and X is an anion that bonds to both [18]. There are few possible anions, such as halides, sulfides or nitrides, but the most common one is oxygen [19]. Also, numerous oxide compounds belong to perovskite-based homologous series, like $A_nB_nO_{3n+1}$ Dion-Jacobson, $A_{n+1}B_nO_{3n+1}$ Ruddlesden-Popper and others [20]. The next chapter is going to focus on ABO_3 perovskite structure, which is investigated in this thesis.

1.1.1 Crystal structure

Around 90 % of the metallic elements of the periodic table are known to be stable in perovskite type ABO_3 structure [21]. This typical structure consists of large-sized 12-coordinated cations at the A site and small-sized 6-coordinated cations at the B site. There have been a lot of differently charged combinations of cations in the A and B- sites, like 1+5, 2+4 or 3+3 [22].

The ideal perovskite structure is a cubic lattice, which can be seen in Figure 1.
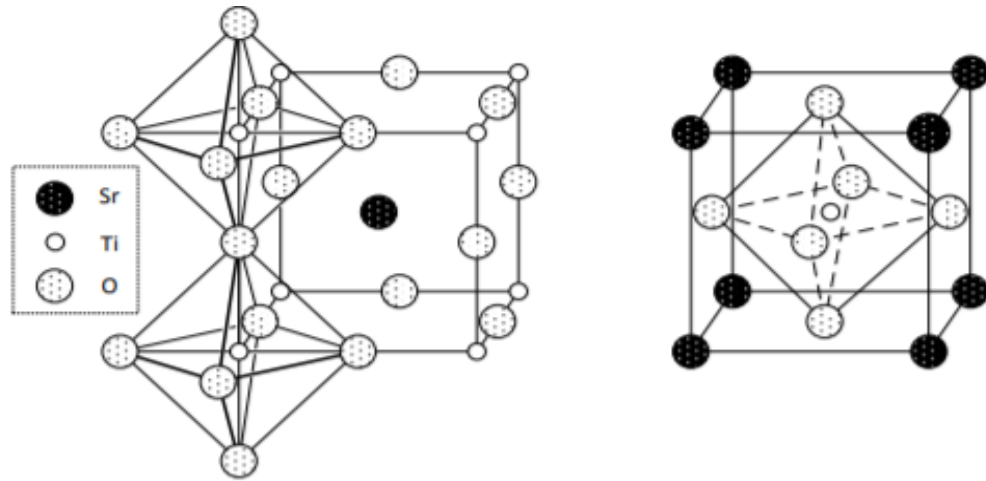
Figure 1. The ideal cubic perovskite structure [30].

This structure can be realized in $CaRbF_3$ or $SrTiO_3$ compounds [18]. According to Figure 1, the A site is occupied by Sr^{2+} cation and B site is occupied by Ti^{4+} cation. Sr^{2+} and O^{2-} ions form a cubic closed-packed lattice and in the octahedral holes created by oxygen anions Ti^{4+} ions can be found. The ideal perovskite structure has a three-dimensional net of corner sharing octahedra (TiO_6 in $SrTiO_3$ case). Only few compounds have this ideal structure, and most of the oxides have distorted structures with lower symmetries, like hexagonal or orthorhombic $YMnO_3$, rhombohedral $BiFeO_3$, tetragonal $BiAlO_3$ etc [23–25]. Furthermore, in some compounds a large extent of oxygen or cation deficiency can be observed [26]. The perovskite structure has various distortions, which strongly affect physical properties of the compounds.

Cell parameter a of ideal perovskite is geometrically related to ionic radii (r_A, r_B and r_O) and can be expressed by equation (1):

$$a = \sqrt{2}(r_A + r_O) = 2(r_B + r_O) \tag{1}$$

The deviation from the ideal structure can be characterized with so-called tolerance factor t [27]; it is described by equation (2):

$$t = \frac{(r_A + r_O)}{\sqrt{2}(r_B + r_O)} \qquad (2)$$

This parameter can vary from 0.80 to 1.1 [22]. In the ideal perovskite structure the t is equal to 1. If the A ion is smaller than the ideal value, then t parameter becomes smaller. Oxides with t values lower than 0.8 can crystallize in the polymorph of perovskite structure, called ilmenite [28]. When t parameter is in the range from 0.89 to 1.00 the oxides has the cubic structure [29]. If the t value higher than 1 the structure becomes hexagonal and if lower than 0.89 – structure is rhombohedral or orthorhombic. Figure 2 demonstrates the crystal groups for $A^{2+}B^{4+}O_3$ and $A^{3+}B^{3+}O_3$ combinations, related to deviation from the ideal structure. The ratio of ionic radii of the A and B cations and the nature of A and B atoms are the main factors in the stability and space group of perovskites.
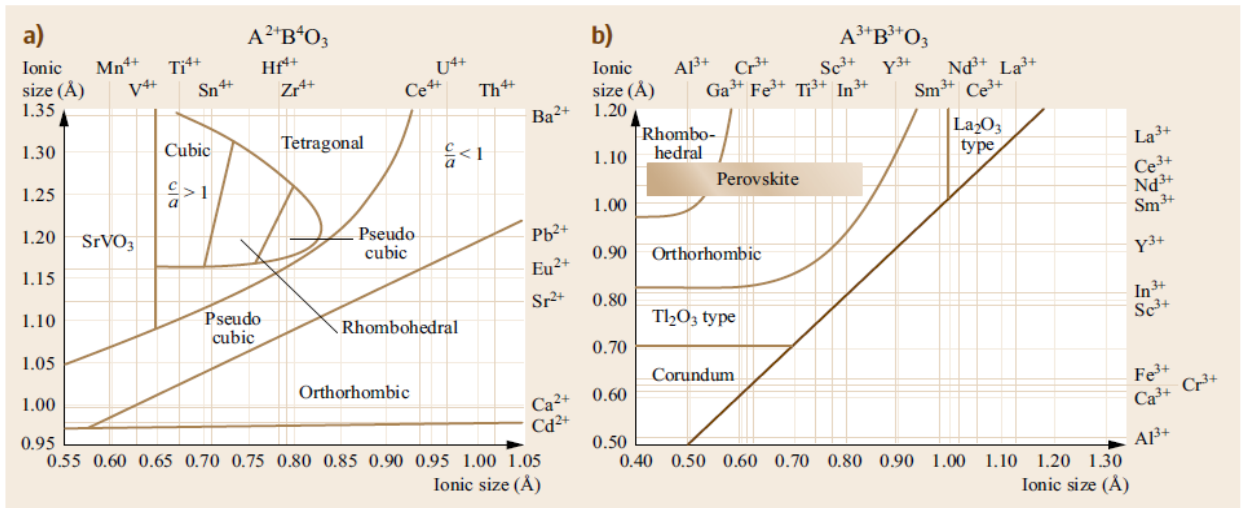

Figure 2. The effect of ionic size of A and B cations on the observed perovskite structure symmetries; (a) $A^{2+}B^{4+}O_3$ (b) $A^{3+}B^{3+}O_2$ [18].

1.1.2 Physical properties

Due to high variety of different structures and chemical compositions, perovskite materials display large variation of physical properties. Some of well-known properties of perovskites are piezoelectricity in $PbTi_{1-x}Zr_xO_3$ and ferroelectricity in $BaTiO_3$-based compounds [31,32]. Superconductivity, ferromagnetism, ionic and electronic conductivity were also observed in the perovskites [33].

1.1.2.1 Dielectric, piezoelectric, ferroelectric and magnetic materials

Dielectric or electrical insulating material can be described as a material in which electric charges do not flow throughout all material, when it is placed in the electric field. These kind of materials do not have free electrons, which can drift through the material [34]. Instead, process called electric polarization can be observed. Positive charges are displaced minutely in the direction of applied electric field and negative charges – in the opposite direction to the electric field. This charge separation causes the reduction of electric field within dielectric [5]. Placing dielectric material into

6

space between two oppositely charged electrodes can significantly increase capacitance of a capacitor [35].

Dielectric constant is used to characterize the amount of electric potential energy, in the form of induced polarization that is stored in a given volume of material when electric field is applied [36]. High permittivity of dielectric material allows greater amount of charge stored at a given volume. Materials as glass, porcelain and some polymers (polyethylene, silicone, epoxy and etc.) are commonly used as dielectrics [37]. Perovskites are also investigated as suitable materials for electrical insulation. Single phase oxides like $SrTiO_3$, $SrZrO_3$ or $BaTiO_3$ and also various solid solutions, for example $AFe_{0.5}B_{0.5}O_3$ (where A=Ba, Sr, Ca; B=Nb, Ta, Sb), are some of examples dielectric materials [38–40].

Other important property of perovskites is piezoelectricity. Piezoelectricity can be described as property of solid materials, when electric charge can be accumulated in response to applied mechanical stress. There are also known inverse piezoelectric effect, when material can deform up on electric field [41]. Crystals with sufficiently low symmetry produce electric polarization under the influence of external mechanical force. Out of 32 space groups 21 are non-centrossymetric and only one of them is not considered as piezoelectric [42]. $PbTi_{1-x}Zr_xO_3$ ceramics are known for high piezoelectricity and still are the most commonly used piezoelectric material [32]. Due to environmental concern of lead-based materials, other solid solutions, like $(K, Na)NbO_3$ or $(1-x)Bi_{0.5}Na_{0.5}TiO_3$-$xBaTiO_3$ were developed for this purpose [4]. Unfortunately, none of them show properties similar to lead-based ceramics.

Ferroelectricity is another interesting feature of perovskites. It can be described as separation of negative and positive electric charges in some dielectrics or non-conducting crystals, that can be reversed by application of electric field [43]. Ferroelectrics can exhibit electric dipole moment in the absence of external electric field. A ferroelectric crystal can be divided in domains, which have different directions of polarization [44]. There are a lot of similarities between ferroelectrics and ferromagnets and one of them is hysteresis loops, which can be observed for both type of materials [45]. Most ferroelectric materials can undergo a structural phase transition from a high-temperature paraelectric phase into a low-temperature ferroelectric phase [46]. The temperature at which this process occurs is called Curie temperature. $BaTiO_3$ is the most investigated ferroelectric material. It has Curie temperature 120 °C and therefore $BaTiO_3$ is ferroelectric at room temperature. It has tetragonal structure at room temperature and above 120 °C the structure becomes non-ferroelectric cubic [47]. Other materials, which have shown this kind of properties are $SrTiO_3$, $KTaO_3$, $KNbO_3$, solid solutions of $Sr_{1-x}Ba_xTiO_3$ etc [48].

Magnetism is defined as a physical property of some materials, which have ability to attract or repel other materials. Magnetic behavior can be classified into five major groups: paramagnetism, diamagnetism, ferromagnetism, antiferromagnetism and ferrimagnetism [49]. All of these five groups react differently when external magnetic field is applied. For instance, diamagnetic materials are repelled by the presence of magnetic field, paramagnetics have unpaired electrons, which tend to align themselves in the same direction of the applied field [50]. Moreover, ferromagnet also has unpaired electrons, which likewise tend to align themselves in the same direction of the external magnetic field. But in these materials there are tendency for magnetic moments to orient parallel to each other to maintain a lowered-energy state [51]. Antiferromangetic solids exhibit different behavior in an applied magnetic field depending upon the temperature. At very low temperatures, the solid exhibits no response to the external field, because the antiparallel ordering of atomic magnets is rigidly maintained.

At higher temperatures, some atoms break free of the orderly arrangement and align with the external field. Ferrimagnetic materials are attracted by magnetic field compared to ferromagnetic substances, due to unequal number of domains, which are aligned in parallel and anti-parallel directions [52]. The transition from ferromagnetic or ferrimagnetic state to paramagnetic state can also be observed for these kinds of materials at temperature known as Curie temperature. Neel point is used to describe transition from antiferromagnetic to paramagnetic state [53].

One interesting group of perovskites, which attracts more attention and shows high variation of unusual states, is $RMnO_3$ (where R - rare earth element). Colossal magnetoresistance was discovered in a hole-doped $LaMnO_3$, and discovery of multiferroicity in $YMnO_3$ and $DyMnO_3$ have caused an increased interest in manganite perovskites [54,55]. The mismatch of R-O and Mn-O bond lengths, where lattice adjusts to the mismatch by tilting of the MnO_6 octahedra, is one of the reason of distortions from ideal cubic structure. Another one – Jahn-Teller (JT) distortion of the MnO_6 octahedra [56]. The Jahn–Teller theorem basically states that any non-linear molecule with a spatially degenerated electronic ground state must experience a geometric distortion that removes the degeneration, as the distortion decreases the species' overall energy [57]. Below T_{JT} the JT distortion becomes static and long-range. It was observed that JT distortion increases with decreasing of r_R from R=La (where T_{JT} ~750 K) to R=Dy (where T_{JT} ~1500 K) [58, 59].

It was expected that magnetic order evolves smoothly with r_R. But it is not the case, which can be observed in Figure 3a). For R=La, the-in plane orbital order induces an A-type antiferromagnetic order with T_N= 140 K, which can be observed in figure 3b). T_N decreases with decreasing of r_R for R=La-Gd, as expected from increased distortion [60,61]. However, the A-type antiferromagnetic structure is no longer the stable ground-state structure for R=Tb and Dy, where sinusoidal incommensurate structure transforms to transverse spiral structure on cooling [51,62]. This spiral structure breaks the inversion symmetry, leading to magnetoelectric effects and ferroelectricity in R=Tb and Dy [55,63].
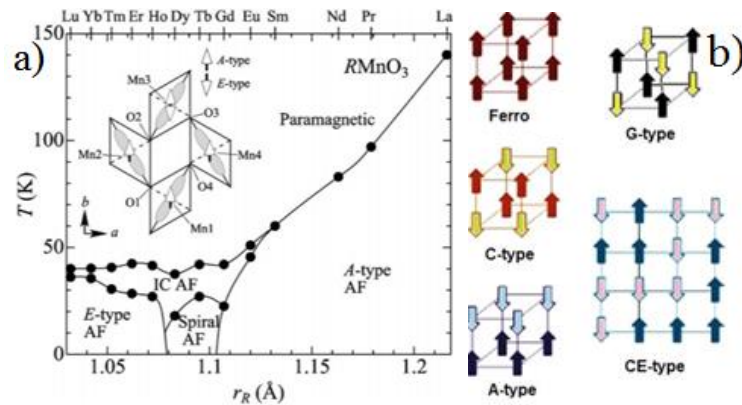
Figure 3. Magnetic phase diagram for $RMnO_3$ as a function of the ionic radius of R (r_R) a) [60]. Schematic representations of different types of magnetic ordering b) [64].

1.1.2.2   Multiferroic materials

Multiferroics can be described as materials in which at least two of ferroic orders, including ferroelectricity, ferromagnetism and ferroelasticity, exist simultaneously [65]. In materials, which show ferromagnetism and ferroelectricity at the same time, polarization can be handled by application of magnetic field and magnetization – by application of electric field. Such materials are known as

magnetoelectric materials [66]. Nowadays the term multiferroic is used to label materials in which ferroelectricity are accompanied by ferromagnetic, ferrimagnetic or antiferromagnetic orders in single or multiphase materials [67]. All multiferroic ceramics can be classified into two categories: single phase and composite materials.

Single phase multiferroics are subdivided into type-I and type-II. First type includes lone-pair ferroelectrics, improper geometric ferroelectrics (general formula $RMnO_3$, where R=Ho, Er, Tm, Yb, Lu and Sc), proper geometric ferroelectrics (general formula $BaMF_4$, where M=Mn, Fe, Co, Ni, Mg and Zn) and boracites (general formula $M_3B_7O_{13}X$; M=Cr, Mn, Fe, Co, Cu and X=Cl, Br, I). Ferroelectricity and magnetism exist separately in this type of multiferroics [68]. In second type of multiferroics ferroelectricity is induced by magnetic ordering or charge ordering. This type consists of ferroelectricity due to charge order materials (like $LuFe_2O_4$, RFe_2O_4, where R=Dy, Y and Lu) and ferroelectricity due to magnetic ordering (like $TbMnO_3$, $TbMn_2O_5$) [56]. Composite multiferroics materials can be prepared by combining ferroelectric and ferromagnetic materials. Some examples of multiferroic composites include $NiFe_2O_4$-$Na_{0.5}Bi_{0.5}TiO_3$ or $BiFeO_3$-$xNaNbO_3$ [69,70].

1.1.3 Applications

Due to high variety of different properties, including ferroelectricity, piezoelectricity, dielectricity and others, inorganic perovskite-type oxides have wide ranges of applications, such as information storage devices, gas sensors, fuel cells, catalysis and photovoltaics. Exploiting the multiferroic properties of perovskite for novel multifunctional devices controlled by magnetic and electric fields is very important topic [33]. Magnetoelectric coupling allows to control antiferromangetic vector orientation by an electric field or ferroelectric polarization by a magnetic field [71,72].

Materials, which are used as gas sensors must have qualities, such as convenient electronic structure, good resemblance with target gases, hydrothermal stability, manufacturability and resistance to poison [73]. Properties, like ideal band gap of 3-4 eV, thermal stability and difference in size between A and B cations, which allows various dopants addition, make perovskite a good material for gas sensors [33]. Cobaltates, ferrites and titanates were utilized for gas sensing application for detection of NO_2, CO, methanol, ethanol and hydrocarbons [7,8]. One of the materials, which showed the best CO gas sensing properties, was $LaCoO_3$, prepared by high-energy ball milling. It demonstrated the highest amount of grain boundaries and crystallites with the smallest size of 11 nm compared with other synthesis techniques [7].

Solid oxide fuel cells, where conducting oxide electrolyte is used, can generate heat, electricity and are considered as environmental-friendly and efficient energy conversion devices. There are several types of fuels cells, including alkaline and polymer membrane, which depend on operating temperature, electrolyte type, fuel type and mobile ions [74]. In comparison with other fuel cell, solid oxide fuel cell exhibited distinct properties like low sensitivity to fuel impurities, excellent fuel flexibility, low pollution emissions, cheap materials and high energy conversion efficiency [75]. Perovskites demonstrated properties, like good electronic and ionic conductivity, structural, chemical and thermal stabilities, high catalytic activity towards oxygen reduction, which makes them ideal candidate for electrode material in solid oxide fuel cells [75,76]. Few examples include $Ba_{0.5}Sr_{0.5}Co_{0.8}Fe_{0.2}O_{3-\delta}$ and $Sm_{0.5}Sr_{0.5}CoO_{3-\delta}$, which can be used either as cathode or anode [10,77].

Other important field of application are spin-based electronics, known as spintronics. They offer enhancement over conventional charge-based memory devices which suffers from leakage current, high power usage, device complexity and performance saturation [78]. Giant magnetoresistance and tunneling magnetoresistance are two effects, which are used for magnetic storage and sensing. Giant magnetoresistance is observed in thin films, where ferromagnetic and non-magnetic metallic layers exist. Tunneling magnetoresistance device consists of two ferromagnetic electrodes and a very thin non-magnetic insulator layer. One class of materials which was utilized for spintronics purposes are magnetic oxide materials. Metallic and ferromagnetic solid solutions of $La_{1-x}Sr_xMnO_3$ (where x=0.3-0.4) with combination of $SrTiO_3$ as tunnel barrier were utilized as tunneling magnetoresistance device [11]. Another class includes multiferroic $BiFeO_3$ material [79].

1.2 Single-phase perovskites

Doping the perovskite structure at A or B site can lead to increase in various physical properties, for example electrical conductivity in $(La_{1-x}M_x)CrO_3$ (M = Mg, Ca, Ba for x = 0.3 and M = Sr for x = 0.25) perovskite systems [80]. Before doping, bulk perovskite material requires some consideration regarding its structure and properties. That is why, next chapter is going to focus on bulk perovskite materials, which were used to prepare solid solutions.

1.2.1 LaMnO₃

Stoichiometric $LaMnO_3$ at room temperature has orthorhombic crystal structure. The oxygen content in this perovskite depends on few factors, which include synthesis temperature, heating duration and atmosphere [81,82]. The cationic vacancies are used to explain the excess of oxygen. The $LaMnO_{3+\delta}$ material structure is orthorhombic when $0 \leq \delta \leq 0.06$, and transforms to rhombohedral when $0.10 \leq \delta \leq 0.18$. For the intermediate range from 0.06 to 0.10, for the sample with δ=0.07 reflections of both phases were observed in XRD patterns [82].

These materials exhibit ambiguous physical properties related to complex interplay between magnetic, orbital, charge and structure of freedom. This includes a various phases with different structural, magnetic, transport properties and also colossal-magnetoresistance effects [83]. Also $LaMnO_3$ is antiferromagnetic insulator with high chemical stability at high temperatures [84]. This compound possesses rich phase diagram depending on the doping concentration, pressure and temperature, being either ferromagnetic metal, charge-ordered insulator or as mention before antiferromagnetic insulator [85].

1.2.2 BiMnO₃

At ambient pressure there are 3 structural modifications of $BiMnO_3$, which are temperature-dependent. At room temperature this compound crystal structure is monoclinic with C2/c space group. First phase transition to another monoclinic structure without detectable change in the symmetry occurs at 474 K, and second transition to orthorhombic phase with Pnma space group at 768 K [86]. First phase transition is accompanied by thermal effect, abrupt changes of lattice parameters and a small jump of resistivity. Moreover, it was observed that not only the structure is temperature dependent but also pressure induces changes in the structure [87]. Furthermore, in similarity to $LaMnO_3$, excess of oxygen was also observed in $BiMnO_3$ [88].

This material is regarded as one of the most prominent multiferroic. $BiMnO_3$ has well entrenched ferromagnetism with Curie temperature being about 100 K and saturation magnetization of

3.92 μ_B per formula unit, which is close to expected 4 μ_B for fully saturated ferromagnetic state [89]. Ferroelectric loops was also observed in thin film samples of $BiMnO_3$ [90]. Existence of two sublattices is considered the reason for multiferroic behavior. Firstly, Mn sublattice is responsible for magnetism and activity of $Bi(1s^2)$ lone pairs is believed to be the origin of the structural distortions and inversion center breaking, resulting in ferroelectricity [91]. Preparation of this material at ambient conditions is still complex, and usually it is synthesized using high pressure and temperature.

1.2.3 $SrTiO_3$

As established previously at room temperature $SrTiO_3$ has ideal cubic structure, with tolerance factor being 1. At 105 K it undergoes cubic-tetragonal phase transition with slightly rotated oxygens around z axis, known as antifferodistortive phase [92]. This phase transition is driven by two order parameters. One of them is rotation angle of TiO_6 octahedra that can reach 2.1 ° at 4.2 K [93]. Another one measures the tetragonality of the structure, and is characterized as the a/c ratio [94].

This material demonstrates a semiconducting behavior, good thermal stability, high dielectric constant and also has piezoelectric and paraelectric characteristics, where even without a permanent electric dipole, polarization can be induced by application of an electric field [95]. As a semiconducting material has indirect band gap, which varies from 3.2 to even 3.77 eV [96]. Unlike other ABO_3 type perovskites it has unusual dielectric properties. At higher temperature dielectric response follows Curie-Weiss law, which suggests ferroelectric phase transition at about 35-40 K. But the dielectric constant constantly increases when the temperature rises down and attains maximum value at 4 K [97].

1.2.4 $BaTiO_3$

At room temperature $BaTiO_3$ has tetragonal crystal structure with P4mm space group. When cooled at ambient pressure it has few first-order phase transitions: cubic ($Pm\overline{3}m$) $\xrightarrow{\sim 131\,°C}$ tetragonal (P4mm) $\xrightarrow{\sim 0\,°C}$ orthorhombic (Amm2) $\xrightarrow{\sim -90\,°C}$ rhombohedral (R3m) [98]. The appearance of spontaneous polarization in this structure is related to a shift of Ti^{4+} and O^{2-} ions relatively to Ba^{2+} at the origin. This spontaneous polarization is followed by changes of the unit cell, which are demonstrated in Figure 4.
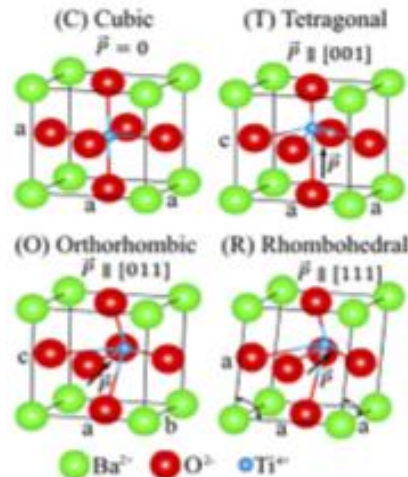

Figure 4. Crystal structure of $BaTiO_3$ polymorphs [99].

The phase transition from cubic to tetragonal phase at Curie temperature is also known as paraelectric-ferroelectric transition [99]. $BaTiO_3$ shows several properties, including optical properties, ferroelectricity, piezoelectricity, pyroelectricity and dielectricity [100]. Also, unique characteristic,

known as positive temperature coefficient of resistivity was observed in this kind of material, doped with La^{3+}, Y^{3+}, Sb^{3+} and Nb^{5+} ions. At room temperature single-phase $BaTiO_3$ is insulator, but intercalation of these cations cause anomalous increase in resistivity near Curie transition [101]. Furthermore, it was observed that dielectric properties depend on microstructure, especially on grain size. The relative permittivity increases with the decrease in grain size [102].

1.3   Synthesis methods

Numerous synthesis techniques were applied for preparation of ABO_3 type perovskites. Some examples include: precipitation, solid state reaction, combustion, sol-gel, plasma-spray drying, freeze-drying, microwave assisted synthesis and much more [33]. Different methods offer unique advantages, like lower calcination temperature for combustion synthesis or morphology control for hydrothermal route. Next chapter going to pay attention to hydrothermal, conventional solid-state method and techniques applied in this work: sol-gel and sol-gel combustion.

1.3.1   Sol-gel method

Sol-gel method is one of the well-known synthetic approaches to prepare novel metal oxide nanostructures [103]. This process involves four main steps, which are hydrolysis, condensation/polymerization of monomers, particles growth and gel formation [104]. Temperature, pH, reactants concentration and other parameters may influence these four steps. Generally, metal acetates, nitrates and alkoxides are used as the metal precursors for this method. Due to high reaction affinity of alkoxides toward water, they are considered as one of the main precursors for the metal oxide preparation [105]. In aqueous sol-gel technique water is used as a solvent and it provides oxygen, which are necessary for the formation of metal oxide.

Main advantages of this process includes low processing temperature, the use of compounds which do not produce impurities in final products and also ability to control textural and surface properties of materials [104]. Among the drawbacks of this synthesis method one can count large volume shrinkage and cracking during drying, also some alkoxide precursors, which are used in this kind of method are costly.

Different kind of gelation and complexing agents are employed in sol-gel method, including citric acid, EDTA, tartaric acid, ethylene glycol, malic acid etc [106,107]. It was shown, that aqueous sol-gel synthesis route is capable of preparing different composition perovskite materials, including $GdAlO_3$, $LaCoO_3$, $LaMoO_3$, $La_xSr_yV_zO_3$, $La_xSr_yMo_zO_3$ or $LaMo_xV_{1-x}O_{3+\delta}$ [106,107]. This method can be applied for preparation of pure monophasic perovskites, with lower calcination temperatures compared with other methods.

1.3.2   Sol-gel auto-combustion method

Sol-gel auto-combustion method involves exothermic and thermally-induced anionic redox reaction of xerogel, which is obtained from aqueous solution containing desired metal salts [108]. The valences of the reacting elements are usually used for calculation of proportions between complexant and salts in order to supply the relation of oxidizer/reductant equal to 1 [109]. Nitrate salts are considered as the main precursors for this kind of reaction, because of the high solubility in water and also NO_3^- ions serve as oxidant source for synthesis [110].

There are number of complexing agents and fuels employed in this method, like glycine, urea, citric acid, hydrazine, acrylic acid etc [111]. There are cases, where no solution is required for sol-gel

auto-combustion synthesis. Metal nitrates and complexant are directly and intensively mixed together while heating. The precursors possess hygroscopicity, which allows them to absorb moisture and become slurry. This combustion method are known as flash-combustion method [112].

Several advantages of sol-gel auto-combustion method involves high product purity and cristallinity, fine particle size and narrow particle size distribution, stoichiometry control, low processing time, there are no multiple steps involved, for example drying, good chemical homogeneity and dopants can be easily introduced in to the structure [113].

This method was successfully utilized for the synthesis of high-quality single and mixed-metal oxide materials with magnetic and electrical properties [114,115]. Different bi- and tri-metallic manganites with magnetic properties were also prepared by sol–gel combustion using glycine–nitrate method [116].

1.3.3 Solid-state reaction

Solid-state can be understand as a process between or within solid reactants to yield a solid product. The reaction occurs in few steps such as nucleation, matter transfer across phase boundaries and diffusion in the reaction product [117]. The high reaction temperature is thermodynamically required for this type of reaction to occur. Furthermore, there are three factors, which influence the rate of reaction between solids: the contact area between reactants, product phase nucleation rate and rate of ions diffusion through the product phase [118].

There are few advantages of solid-state reactions over other method. For example, elimination of solvent means the product cost is lower, also higher reaction yield, environmentally friendly process, with no additional waste to eliminate after the reaction. Although there are a lot of benefits of these type reactions, there are also many drawbacks. The limited possibility of in-situ monitoring of the reaction progress is one of the disadvantages. Furthermore, undesirable phase formation, difficulty of achieving homogeneous distribution of dopants and volatization of reacting mixture at higher temperatures are main drawbacks of this reaction [119].

The metal oxides, carbonates and nitrates are mainly used as precursors for perovskite synthesis. The preparation route consists of mixing precursors by milling in appropriate media of acetone or isopropanol and then calcining at high temperature to allow interdiffusion of the cations [120]. Usually, there are several calcination and milling steps in this type of synthesis. $SrTiO_3$, $SmCoO_3$, $BiMnO_3$ and $BiScO_3$ are only few examples of perovskite material, which was prepared by this technique [121-123].

1.3.4 Hydrothermal synthesis

The term hydrothermal refers to any heterogeneous reaction in the presence of aqueous solvents or mineralizers (like NaCl, NaOH) under high pressure and temperature conditions to dissolve or recrystallize materials that are relatively insoluble under ordinary conditions [124]. Most of hydrothermal reaction occur when the pressure is greater than 1 atm and temperature higher than 100 °C, but some reaction can happen using milder conditions [125]. Suitable apparatus, called autoclaves, are being used in these types of conditions. It is composed of few key parts, for example liner, shell, which are made of materials according to experimental temperature and pressure conditions and the corrosion resistance in that pressure temperature range in a given solvent.

Reaction medium is another important factor in this synthesis. Water as environmentally-friendly, cheap and safe material is used most frequently as reaction medium. Viscosity and dielectric

constant of water are decreasing with increase of the temperature. Under normal conditions, electrolyte will be totally dissociated in water. However, the dissociated ions will tend to recombine together with rising temperature and for most of the substances this transition will occur at 200-500 ℃ [126]. Furthermore, due to decrease of viscosity the mobility of molecules and ions in water under hydrothermal condition is much higher than under normal conditions.

The hydrothermal technique is ideal for the processing of very fine powders having high purity, controlled stoichiometry, narrow particle size distribution, controlled morphology, uniformity, less defects, high crystallinity, excellent reproducibility, controlling of microstructure etc. Main drawbacks are complicated design and cost of some autoclaves, cumbersome operations like assembling and dissembling, impossible to observe the actual process [127].

Hydrothermal method is capable for preparing perovskite materials with different kind of morphology and composition. It was observed that, mineralizer KOH concentration in $BiFeO_3$ synthesis can result in different particle formation, beginning with walnut-shaped microspheres at lowest concentration and leading to honeycomb shaped particles [128]. Furthermore, tetragonal $CaTiO_3$ microrods, cube-shaped Li-doped $PbTiO_3$ or $La_{0.5}Ba_{0.5}MnO_3$ and $BaTiO_3$ or $SrTiO_3$ nanotubes can be prepared [129–131].

2. EXPERIMENTAL

2.1 Reagents

For the synthesis of compounds which were investigated in this work lanthanum(III) nitrate hexahydrate (La(NO$_3$)$_3$·6H$_2$O, Alfa Aesar, 99.9%), manganese(II) nitrate tetrahydrate (Mn(NO$_3$)$_2$·4H$_2$O, Alfa Aesar, 99.9%), bismuth(III) nitrate pentahydrate (Bi(NO$_3$)$_3$·5H$_2$O, Roth, 98%), citric acid monohydrate (C$_6$H$_8$O$_7$·H$_2$O, Chempur, 99.9%), barium acetate (Ba(CH$_3$COO)$_2$, Chempur, ≥99%), titanium(IV) isopropoxide (C$_{12}$H$_{28}$O$_4$Ti, Sigma-Aldrich, ≥97%), nitric acid (HNO$_3$, Reachem s.r.o. 65%,), ethylene glycol (C$_2$H$_6$O$_2$, Sigma-Aldrich, ≥99.5%) and strontium nitrate (Sr(NO$_3$)$_2$, Sigma-Aldrich , 99.9 %) were used as starting materials.

2.2 Synthesis

For the preparation of B$_{ix}$La$_{1-x}$MnO$_{3+\delta}$ samples by sol–gel combustion synthesis route the appropriate amounts of metal nitrates and citric acid monohydrate (the ratio between metal nitrates and citric acid monohydrate was 1:0.83 [132]) were mixed in a beaker at 80 °C until crystalline water was released and clear solution was formed. Citric acid monohydrate was used as a complexing agent and fuel for the self-burning reaction. The obtained mixture was stirred for 1 h, afterwards the sol was transformed into transparent gel by slow evaporation of water at 100 °C. In this stage of sol–gel processing, the temperature of the hot plate was increased to 250 °C and spontaneous ignition process took place. Finally, the ashes were collected and annealed in a furnace for 6 h at 1000 °C in air atmosphere with a heating rate of 5 °C/min. The reaction scheme is represented in Figure 5.

For the synthesis of BTO-BMO solid solutions required amount of citric acid monohydrate was dissolved in 20 ml of distilled water following by addition of titanium isopropoxide. The beaker was heated on a hot plate at 90 °C and the mixture was stirred until a clear and transparent solution was obtained. During the next stage, Mn(NO$_3$)$_2$·4H$_2$O and Ba(CH$_3$COO)$_2$ were added to the above solution and dissolved rapidly. Prior to addition of Bi(NO$_3$)$_3$·5H$_2$O, pH value of the reaction mixture was adjusted to approximately 1 by adding nitric acid in order to prevent formation of precipitates. After dissolution of all precursors clear and transparent solution was obtained and appropriate amount of ethylene glycol was added (total metal ions to citric acid to ethylene glycol molar ratio was 1: 3: 10). The obtained multielement precursor solution was homogenized under constant stirring at 90 °C for 1.5 h in a beaker covered with a watch glass. After this time the resulted solution was concentrated by evaporation of solvent at 150 °C until it turned into a viscous gel. The resulted gel was dried in the oven at 180 °C for 12 h, carefully ground in a mortar and annealed at 1000 °C for 5 h in air atmosphere with a heating rate of 5 °C/min.

In the case of STO-BMO solid solutions, reaction was performed in similar path like for BTO-BMO, except Sr(NO$_3$)$_2$ was used instead of Ba(CH$_3$COO)$_2$. The reaction scheme for both solid solution systems is demonstrated in Figure 6.

```
┌─────────────────────────────────────────────────┐
│  Bi, La, Mn nitrates + Citric acid monohydrate    │
└─────────────────────────────────────────────────┘
                      │
                      │        ┌──────────────────────────────────┐
                      │        │  Mixed at 80 °C until water release │
                      ▼        └──────────────────────────────────┘
┌─────────────────────────────────────────────────┐
│                 Clear solution                    │
└─────────────────────────────────────────────────┘
                      │
                      │        ┌──────────────────────────────────┐
                      │        │       Mixture stirred for 1 h       │
                      ▼        └──────────────────────────────────┘
┌─────────────────────────────────────────────────┐
│                      Sol                          │
└─────────────────────────────────────────────────┘
                      │
                      │        ┌──────────────────────────────────┐
                      │        │   Evaporation of water at 100 °C    │
                      ▼        └──────────────────────────────────┘
┌─────────────────────────────────────────────────┐
│                      Gel                          │
└─────────────────────────────────────────────────┘
                      │
                      │        ┌──────────────────────────────────┐
                      │        │  The temperature increased to 250 °C │
                      ▼        └──────────────────────────────────┘
┌─────────────────────────────────────────────────┐
│                     Ashes                         │
└─────────────────────────────────────────────────┘
                      │
                      │        ┌──────────────────────────────────┐
                      │        │ Annealed in a furnace for 6 h at 1000 °C │
                      ▼        └──────────────────────────────────┘
┌─────────────────────────────────────────────────┐
│                 Bi$_x$La$_{1-x}$MnO$_3$            │
└─────────────────────────────────────────────────┘
```
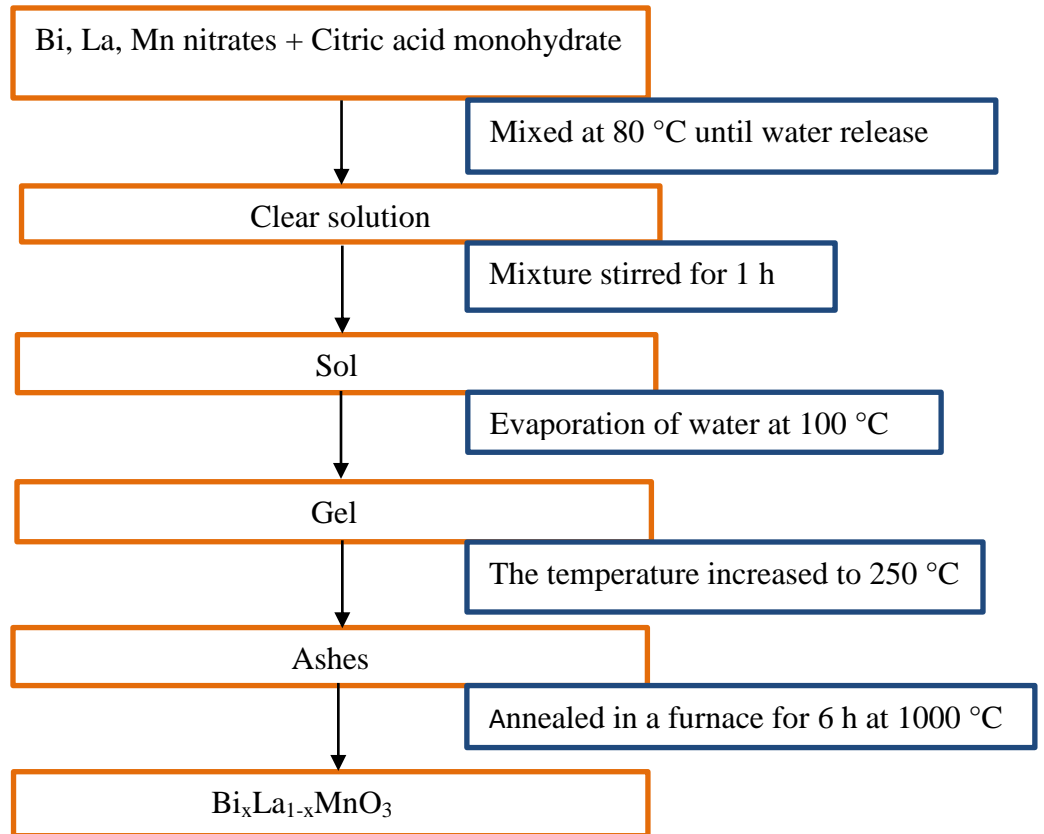
Figure 5. Principal scheme of the synthesis of $B_{ix}La_{1-x}MnO_{3+\delta}$ solid solutions by sol-gel combustion method.
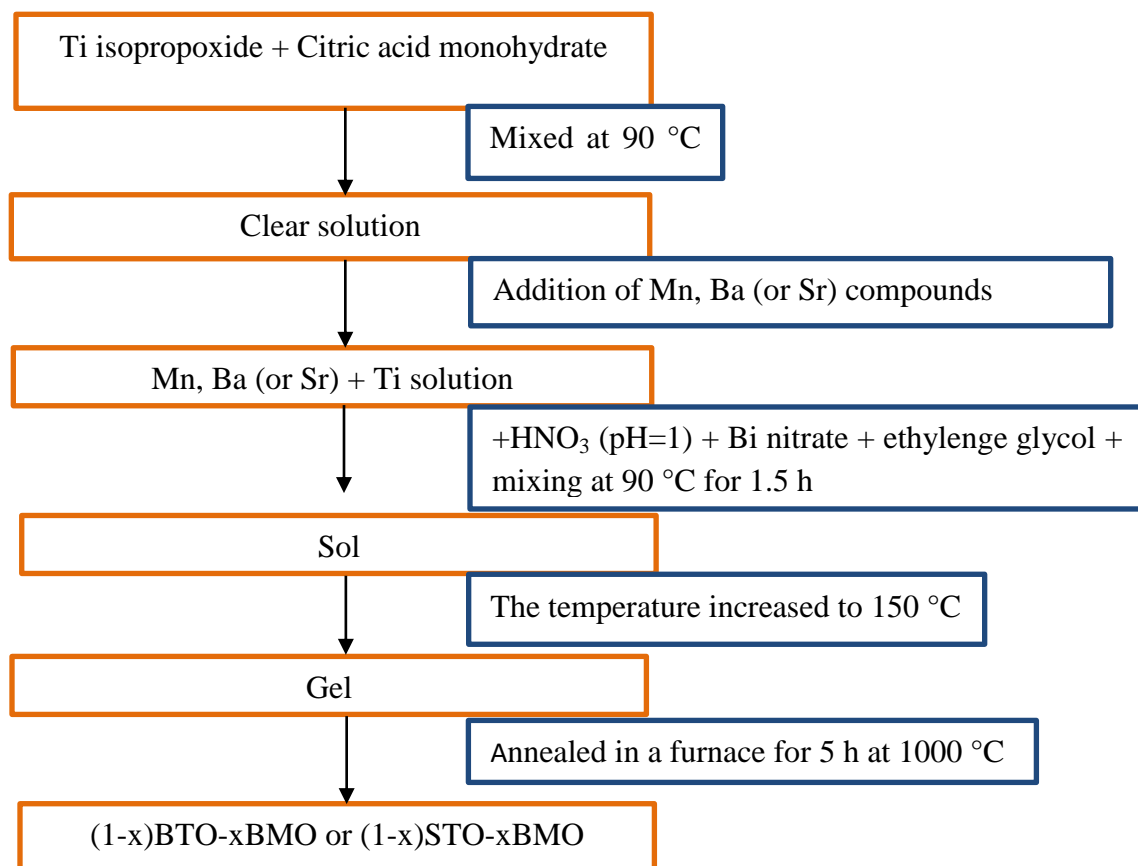
```
┌─────────────────────────────────────────────┐
│   Ti isopropoxide + Citric acid monohydrate   │
└─────────────────────────────────────────────┘
                     │
                     │        ┌──────────────────┐
                     │        │  Mixed at 90 °C   │
                     ▼        └──────────────────┘
┌─────────────────────────────────────────────┐
│                Clear solution                 │
└─────────────────────────────────────────────┘
                     │    ┌───────────────────────────────────┐
                     │    │ Addition of Mn, Ba (or Sr) compounds │
                     ▼    └───────────────────────────────────┘
┌─────────────────────────────────────────────┐
│          Mn, Ba (or Sr) + Ti solution         │
└─────────────────────────────────────────────┘
                     │
                     ▼
┌─────────────────────────────────────────────┐
│                     Sol                       │
└─────────────────────────────────────────────┘
                     │
                     ▼
┌─────────────────────────────────────────────┐
│                     Gel                       │
└─────────────────────────────────────────────┘
                     │
                     ▼
┌─────────────────────────────────────────────┐
│      (1-x)BTO-xBMO or (1-x)STO-xBMO           │
└─────────────────────────────────────────────┘
```

Figure 6. Principal scheme of the synthesis of (1-x)BTO-xBMO and (1-x)STO-xBMO solid solutions by sol-gel method.

2.3 Characterization

Thermal decomposition of precursor gels was investigated by thermogravimetric and differential scanning calorimetric (TG-DSC) analysis using PerkinElmer STA 6000 Simultaneous Thermal Analyzer. About 5–10 mg of dried sample was heated from 30 °C to 900 °C at 10 °C/min heating rate in a dry flowing air (20 mL/min). X-ray diffraction (XRD) analysis of obtained products were performed with Rigaku Miniflex II diffractometer using a primary beam Cu Kα radiation ($\lambda = 1.541838$ Å). The 2θ angle of the diffractometer was set in the range from 10° to 80° with a step of 0.02°and measuring time of 0.4 s per step. The obtained diffraction data were refined by the Rietveld method using the Fullprof suite. Bruker-Alpha FT-IR spectrometer was used for FT-IR analysis of compounds. All spectra were recorded at ambient temperature in the range of 4000–400 cm−1. Raman spectra were recorded using inVia Raman (Renishaw, United Kingdom) spectrometer equipped with thermoelectrically cooled (−70 °C) CCD camera and microscope. Raman spectra were excited with 532 nm beam from the CW diode pumped solid state (DPSS) laser (Renishaw, UK). The laser power at the sample was restricted to 0.6 mW. The 20x/0.40 NA objective was used during all the measurements. The overall integration time was 100 s. Position of the Raman bands on the wavenumber axis was

calibrated by the polystyrene film standard spectrum. Parameters of the bands were determined by fitting the experimental spectra with Gaussian-Lorentzian shape components using GRAMS/A1 8.0 (Thermo Scientific, USA) software. The morphology of the samples was examined using a scanning electron microscope (SEM) Hitachi SU-70. The vibrating sample magnetometer was applied for the magnetization measurements. The compounds were encapsulated into a plastic straw and placed into the magnetometer. The lock-in amplifier SR510 was used for measurement of the signal from the sense coils generated by vibrating sample. The gauss/teslameter FH-54 was used to measure the magnetic field strength between the poles of the laboratory magnet, which was supplied by the power source SM 330-AR-22.

3. RESULTS AND DISCUSSION

3.1 $Bi_xLa_{1-x}MnO_{3+\delta}$ solid solutions

The $BixLa_{1-x}MnO_{3+\delta}$ compounds (x = 0.0–0.65) were synthesized by heating the appropriate La–Bi–Mn–O precursor gel. The thermal decomposition behavior of Bi(0.6)–La(0.4)–Mn–O dried gel was investigated using TG/DTG/DSC measurements in order to determine the decomposition steps and possible final annealing temperature (Figure 7). The first mass loss (about 15%) in the TG curve was observed in the temperature range of 30–160 °C and could be attributed to the removal of residual water. The small endotherm in the DSC curve peaked at about 110 °C also indicates this process. It can be seen that thermal decomposition of Bi (0.6)–La(0.4)–Mn-O gel occurs in one main step, which can be associated with combustion reaction. Sharp exothermic peak can be observed at 164 °C in the DSC curve confirming that combustion reaction occurs during thermal degradation of the gel. With further increasing of temperature the mass is nearly constant. After the reaction the total weight of the sample decreased at about 92%.
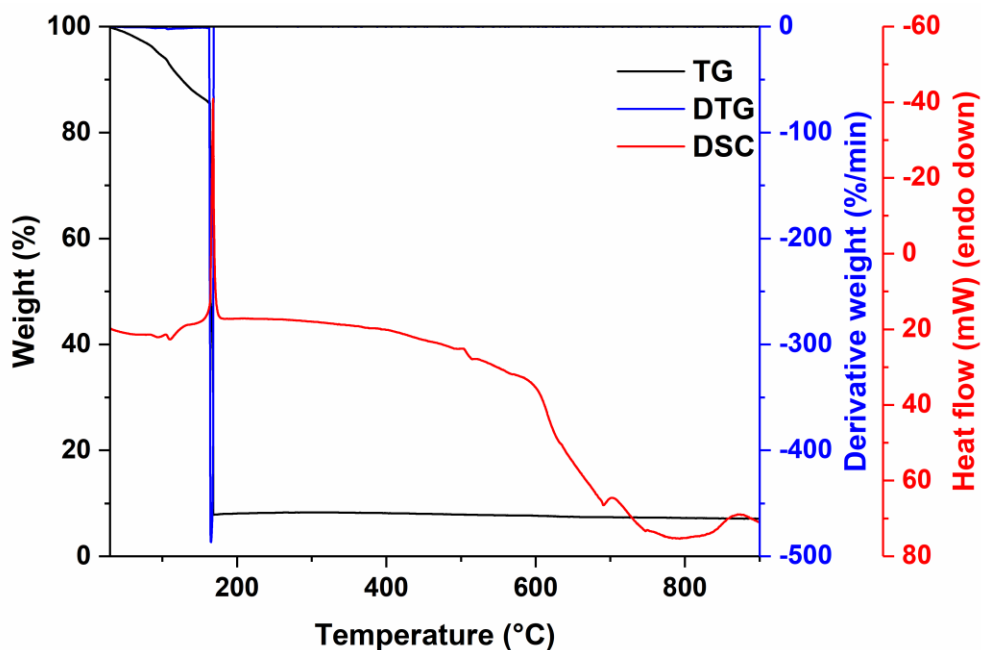
Figure 7. TG/DTG/DSC curves of Bi(0.6)–La(0.4)–Mn–O dried gel.

Figure 8 represents the XRD patterns of sol–gel-derived $Bi_xLa_{1-x}MnO_{3+\delta}$ compounds. It is evident that all synthesized compounds are monophasic and no even traces of impurity phases are present at higher Bi^{3+} concentrations, as was reported previously [133–135]. The Rietveld refinement of the XRD data confirmed the formation of trigonal perovskite structure with hexagonal setting $R\bar{3}c$, which was previously reported [136,137]. The same space group and crystallographic structure were observed for the samples with x = 0.1–0.3. As the amount of Bi^{3+} increased, the shift of all diffraction peaks to lower 2θ values region was observed. Moreover, the intensity of less intense diffraction lines (204), (300), (217), (218), (321), and (330) monotonically decreases, until these peaks completely vanish at x = 0.4. From this point the perovskite structure can be indexed by cubic cell with Pm3m space group. The diffraction peaks (200), (201), and (301) start to split when Bi^{3+} concentration is

19

reached 0.65. This should indicate another structural change, but the sample can still be fitted according to the cubic cell. Taking into account that $BiMnO_3$ is monoclinic, it is expected that symmetry should be further divergent from cubic with further increasing Bi^{3+} amount from 0.65 to 1.0.
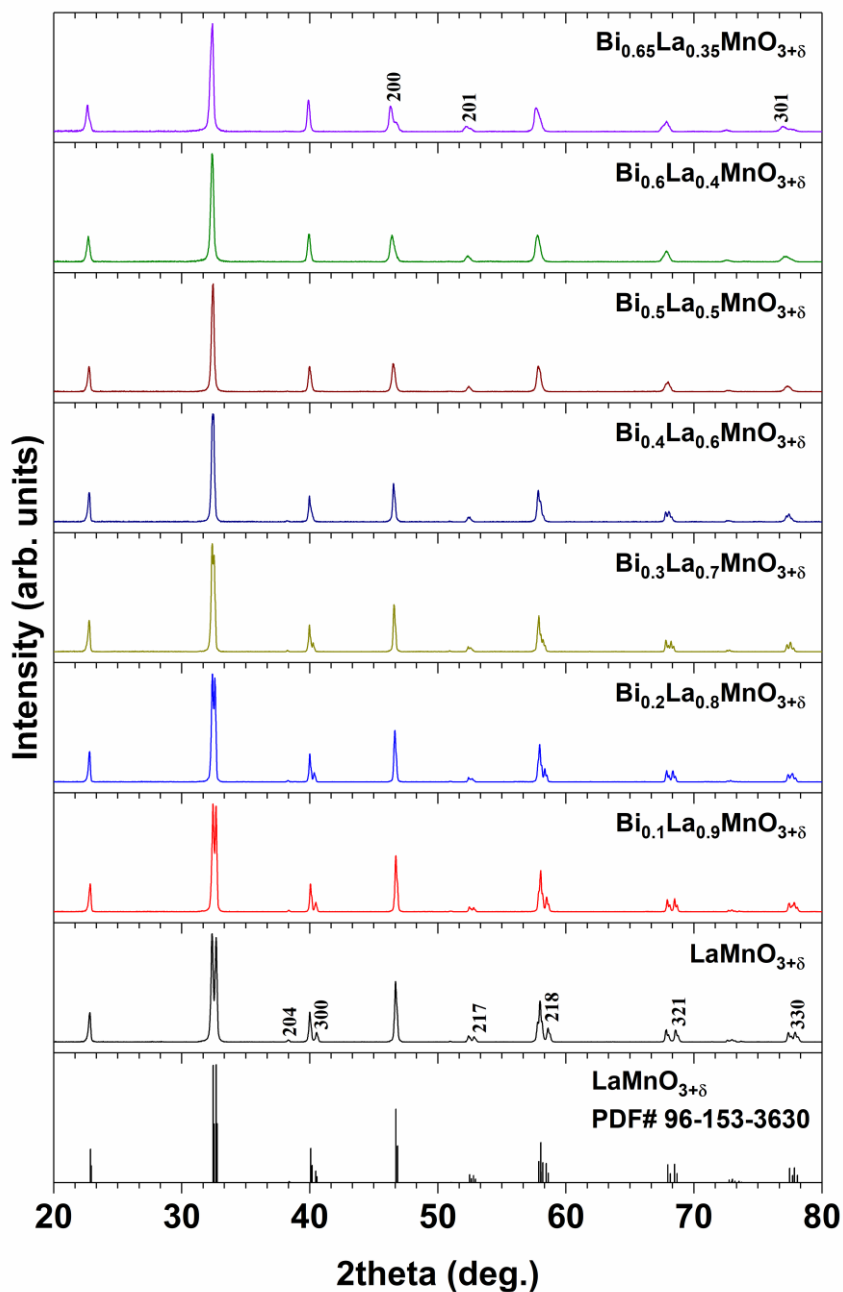

Figure 8. XRD patterns of $Bi_xLa_{1-x}MnO_{3+\delta}$ powders obtained at 1000 °C.

All refined lattice parameters and Mn–O bond lengths for the synthesized samples are presented in Table 1. It is clearly seen that Mn–O bond length, cell parameters and cell volume are slightly different for the samples with different substitutional level of bismuth. These changes probably are caused by slightly different ionic radius of Bi^{3+} (1.17 Å) and La^{3+} (1.16 Å) in eightfold coordination [138]. The parameter a decreases as x increases until x = 0.2. The similar trend was also observed in

20

ref. [133]. The value of parameter a abruptly increases when x reaches 0.3. The observed increase in parameter c in trigonal structure is nearly linear. In the cubic cell the increase of parameter a also can be seen. By comparing the determined cell volumes of cubic and trigonal cells we can conclude that volume in trigonal cell is about six times larger than in cubic cell. In addition, the cell volume increases almost linearly with increasing amount of Bi^{3+} in both types of cells.

Table 1. Lattice parameters and Mn–O bond lengths of $Bi_xLa_{1-x}MnO_{3+\delta}$ samples.

x	a (Å)	b (Å)	c (Å)	V (Å^3)	Mn-O (Å)
0	5.5158 (8)	5.5158 (8)	13.3234 (2)	351.05 (5)	1.9524
0.1	5.5124 (4)	5.5124 (4)	13.3584 (2)	351.53 (9)	1.9600
0.2	5.5120 (6)	5.5120 (6)	13.3760 (8)	351.95 (5)	1.9607
0.3	5.5164 (8)	5.5164 (8)	13.408 (8)	353.38 (3)	1.9566
0.4	3.8960 (9)	3.8960 (9)	3.8960 (9)	59.14 (1)	1.9480
0.5	3.8998 (6)	3.8998 (6)	3.8998 (6)	59.31 (2)	1.9499
0.6	3.9010 (7)	3.9010 (7)	3.9010 (7)	59.36 (8)	1.9505
0.65	3.9070 (8)	3.9070 (8)	3.9070 (8)	59.64 (3)	1.9535

Figure 9 represents FT-IR analysis data of fabricated $Bi_xLa_{1-x}MnO_{3+\delta}$ samples. In perovskite-like ABO_3 structure, cations La^{3+} and Bi^{3+} occupy A sites and Mn^{3+} ions B sites. Six oxygen O^{2-} anions and one manganese cation are forming MnO_6 octahedron. There are six possible vibration modes for this octahedron (three of them are stretching and three of them are vibrating modes) [139]. Only two modes (one bending and one stretching) are infrared active, with frequencies about 600 and 350 cm^{-1}, respectively [139]. The FT-IR spectra presented in Figure 9 clearly show the absorption bands at 560–575 cm^{-1} attributable to the Mn–O stretching vibration in MnO_6. However, no correlation between the changes in Mn–O bond length and vibration frequencies in FT-IR spectra was observed.

The morphology of the synthesized $Bi_xLa_{1-x}MnO_{3+\delta}$ powders was examined using SEM. The SEM micrographs of the representative $Bi_xLa_{1-x}MnO_{3+\delta}$ samples with x = 0, 0.3, 0.6, and 0.65 are shown in Figure 10. The $LaMnO_{3+\delta}$ solids are composed of the polyhedral particles varying in size in the range of ~100–200 nm (Figure 10a). These particles form "dimers" or even "oligomers" showing negligible association and interaction between the grains. It is clearly seen that partial substitution of lanthanum ions by bismuth changes morphology of the powders. Two trends associated with an introduction of bismuth into crystal lattice were observed—first, increase in bismuth content promotes gradual growth of the grains. The second trend is that the particles in the bismuth containing compounds have lost the strict shape and show high tendency for agglomeration. The size of individual grains in $Bi_{0.65}La_{0.35}MnO_{3+\delta}$ increased up to 5–10 μm (Figure 10d).
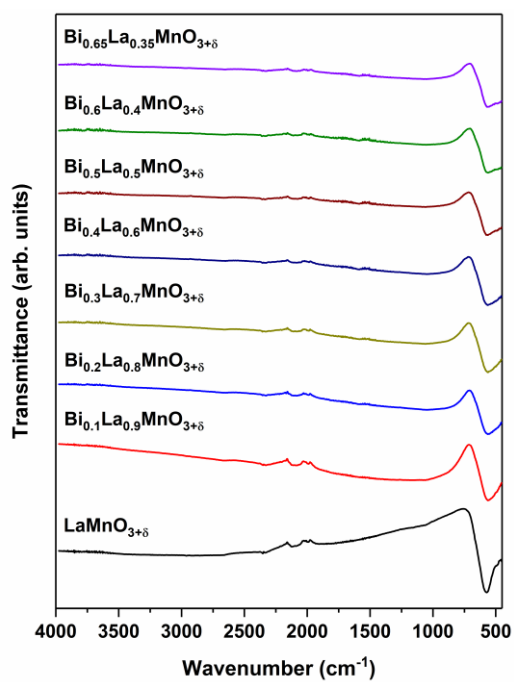
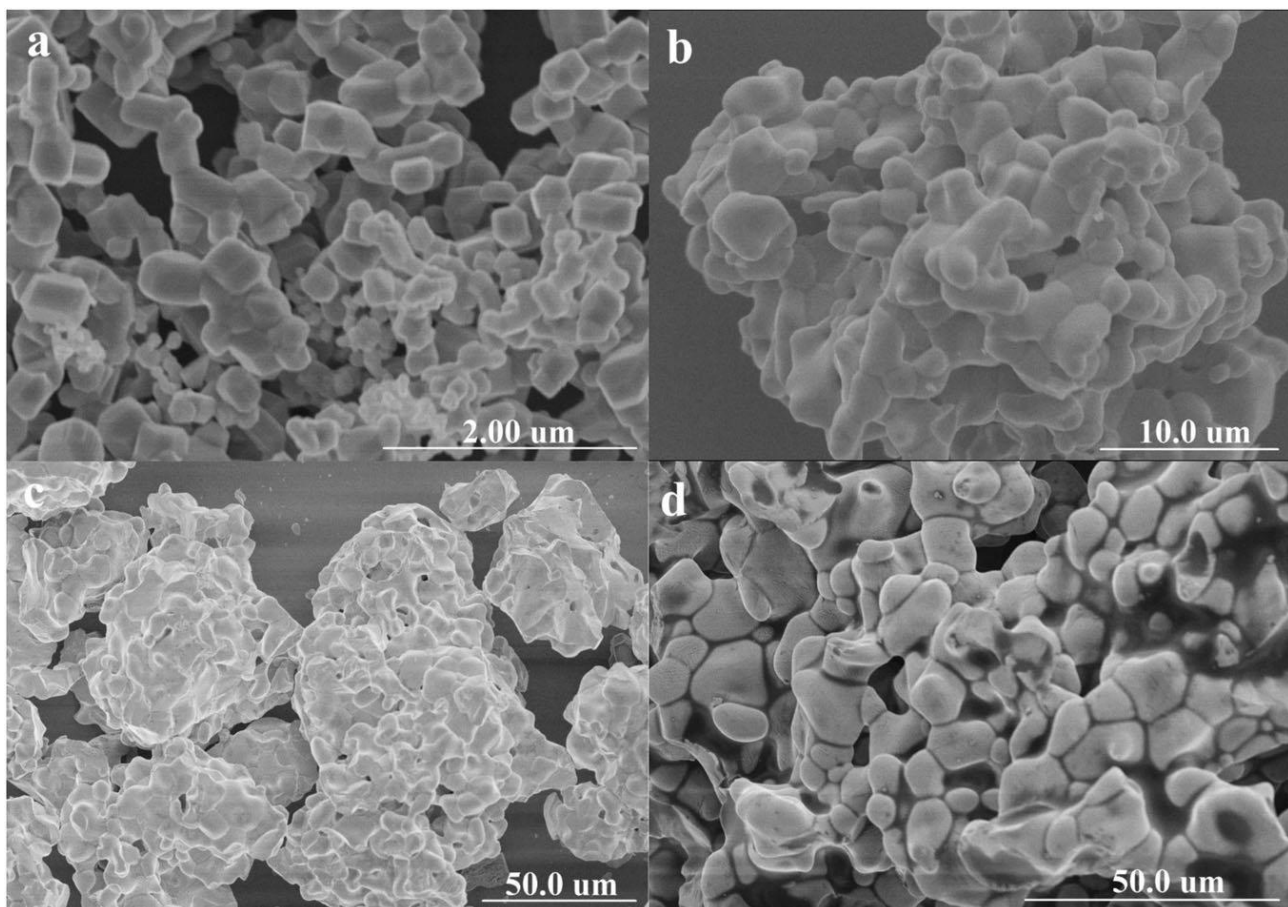Figure 9. FT-IR spectra of $Bi_xLa_{1-x}MnO_{3+\delta}$ samples.

Figure 10. SEM micrographs of $LaMnO_{3+\delta}$ (a), $Bi_{0.3}La_{0.7}MnO_{3+\delta}$ (b), $Bi_{0.6}La_{0.4}MnO_{3+\delta}$ (c), and $Bi_{0.65}La_{0.35}MnO_{3+\delta}$ (d) samples.

The magnetization studies were also carried out for the $Bi_xLa_{1-x}MnO_{3+\delta}$ samples. The corresponding hysteresis curves are represented in Figure 11. For the $LaMnO_{3+\delta}$ sample the Curie transition from ferromagnetic to paramagnetic phase occurs at 140–180 K interval [135,140]. The M–H loops for the sol–gel-derived $Bi_xLa_{1-x}MnO_{3+\delta}$ samples obtained at room temperature are linear, which correspond with previous reported data and indicate the paramagnetic state for all samples. Also, no saturation of magnetization was observed at applied magnetic field. From Figure 11, we can clearly see that magnetization for trigonal structure is about 2–3 times higher than magnetization in cubic structure. It seems that structural transition causes the change in magnetic properties of $Bi_xLa_{1-x}MnO_{3+\delta}$ as well. The magnetization is clearly different determined for the $Bi_{0.3}La_{0.7}MnO_{3+\delta}$ and $Bi_{0.4}La_{0.6}MnO_{3+\delta}$ samples. For trigonal cell magnetization decreases with increasing amount of Bi^{3+} negligibly, with only exception for x=0.1, which is a little higher than for observed for the sample with x=0.2 sample. There is no clear dependence between magnetization and bismuth content in highly doped $Bi_xLa_{1-x}MnO_{3+\delta}$ samples (x from 0.4 to 0.65) with cubic crystal structure as well. The magnetization values vary insignificantly. Different amount of bismuth in the crystal lattice, grain size or morphology of the powders do not show any obvious trends.
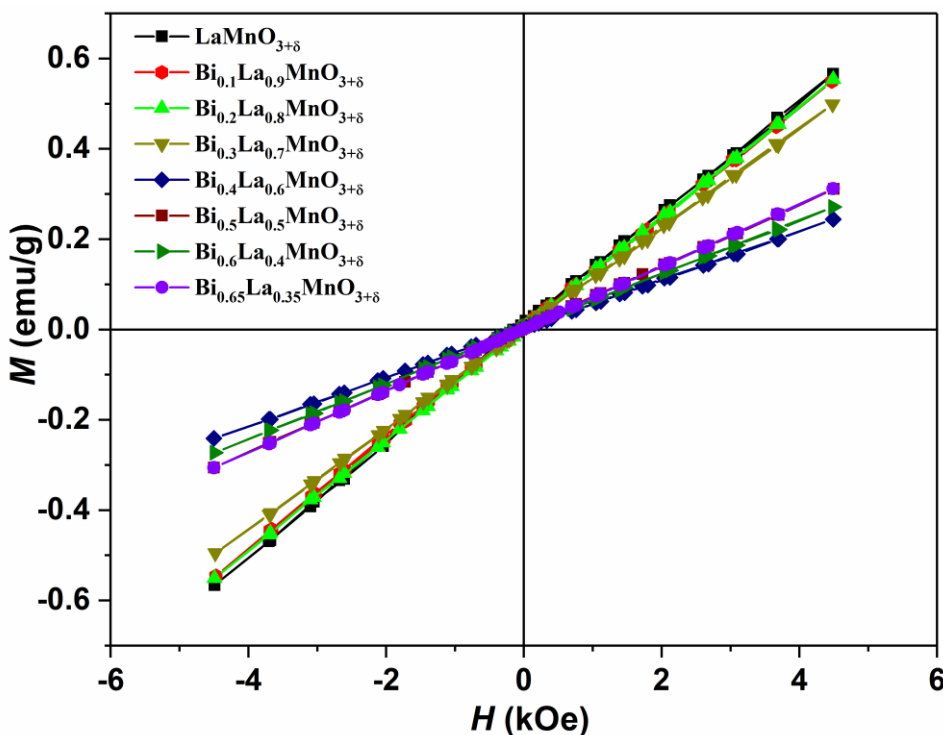

Figure 11. Magnetization versus magnetic field curves for $Bi_xLa_{1-x}MnO_{3+\delta}$ samples.

3.2 BaTiO₃–BiMnO₃ solid solutions

Thermogravimetric analysis was performed in order to investigate thermal decomposition behavior of Ba–Ti–O and Ba–Bi–Ti–Mn–O precursor gels. TG/DTG/DSC curves of the gel corresponding to final BTO product are depicted in Figure 12. It is seen that degradation of precursor gel can be divided into four steps. Initially non-significant weight loss occurred at temperatures below 100 °C, this process is attributed to the removal of adsorbed water. Next, drastic weight loss centered at 260 °C took place, this step is associated with decomposition of nitrates and organic components and

accompanied by a weak exothermic peak in DSC curve. After this, the second clearly visible weight loss accompanied by a strong exothermic signal occurred at around 450 °C. During this step residual organic parts of the gel were decomposed. And the last weight loss can be clearly seen from DTG curve at 750 °C, it could be ascribed to the decomposition of barium carbonate [141,142]. At the above temperatures residual mass was determined to be constant. Total weight loss calculated from TG curve was 82%.
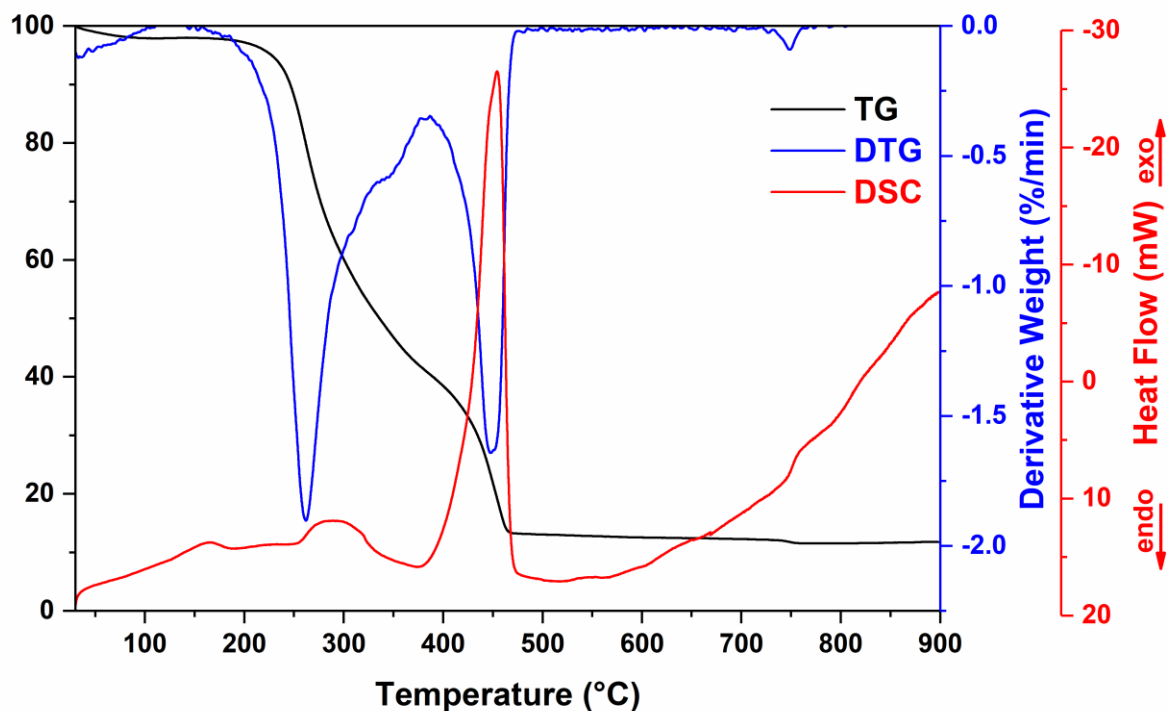

Figure 12. TG/DTG/DSC curves of Ba–Ti–O precursor gel.

Thermal decomposition of the gel containing the highest amount of BMO was studied for comparison (see Figure 13). The degradation took place in a very similar way. Again, initial weight loss at low temperatures was associated with removal of water. The observed temperature of the second decomposition step was slightly lower in comparison to BTO precursor gel and was centered at around 240 °C. The last and the most rapid exothermic decomposition step was detected at 380 °C, which is around 70 °C lower than in the first case. Residual mass remained clearly constant at above 400 °C and no weight change at higher temperatures was observed, which suggests that the last step for Ba–Ti–O gel was probably related to decomposition of $BaCO_3$ species. Total weight loss was comparable with that of BTO precursor gel and was found to be 85 %. Although minimal annealing temperatures determined from TG analysis were relatively low, it was experimentally confirmed that 1000 °C annealing temperature is required for the formation of single-phase final products.
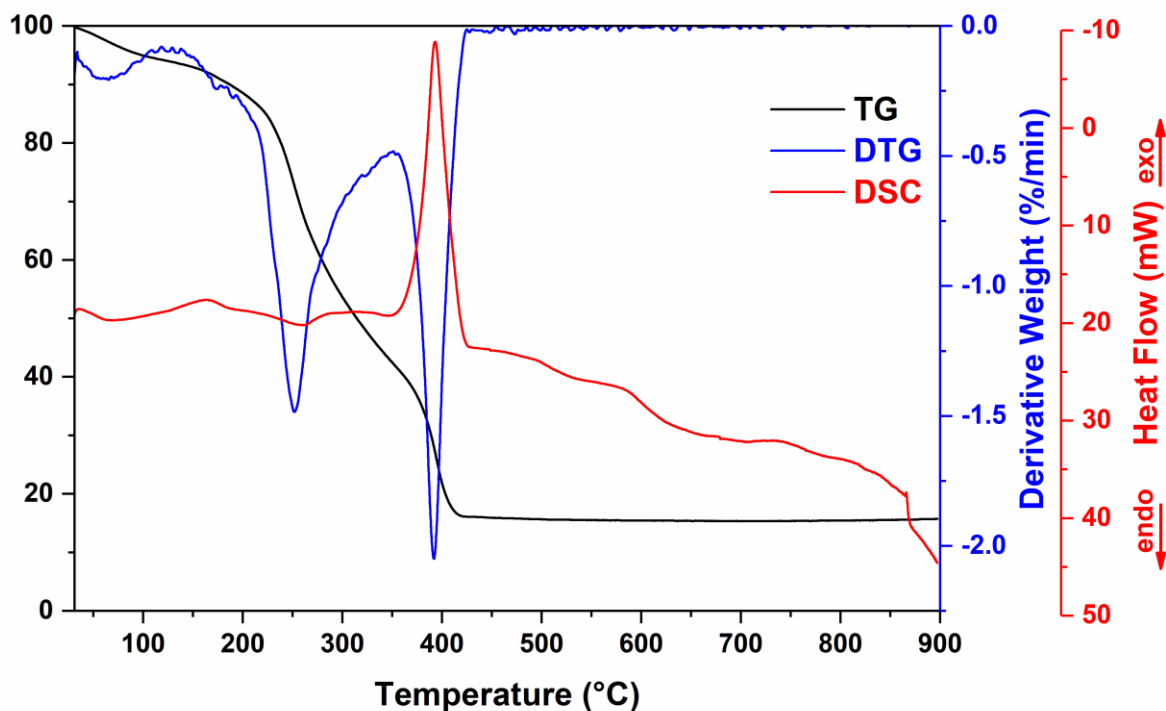
Figure 13. TG/DTG/DSC curves of 0.4(Ba–Ti–O)-0.6(Bi–Mn–O) gel.

The XRD patterns of BTO-BMO solid solutions annealed at 1000 °C are illustrated in Figure 14. Evidently, after the thermal treatment the precursor gel of pristine BTO crystallized into perovskite structure compound. No secondary crystal phases such as TiO_2 or $BaCO_3$ were detected. The shape of the diffraction peak located at around 45° is usually used to distinguish the presence of cubic or tetragonal BTO structures [143]. In our case there was no obvious splitting of cubic (200) peak into tetragonal (200) and (002), however it is still difficult to assign the crystal structure of synthesized BTO powders to either cubic or tetragonal symmetry. Despite of relatively high annealing temperature the obtained reflection peaks are quite broad. Introduction of BMO component into BTO crystal lattice does not cause any visible changes in the XRD patterns. No extra peaks or peak splitting were observed, indicating an absence of structural changes and phase transitions. Moreover, regardless of the chemical composition of the solid solutions, there was no change in the peak positions in the XRD patterns. Possible explanation of such behavior is that A cation was substituted by a smaller ion and at the same time B cation was substituted by a larger ion [138]. Both substitutions are supposed to result in opposite effects, which probably compensate each other. It was determined that singlephase solid solutions can be synthesized up to BMO content of 60 mol%. With higher percentage of BMO some neighboring crystal phases appeared. Similar limiting amount of BMO fraction was previously observerd for $Bi_xLa_{1-x}MnO_{3+\delta}$ solid solutions.
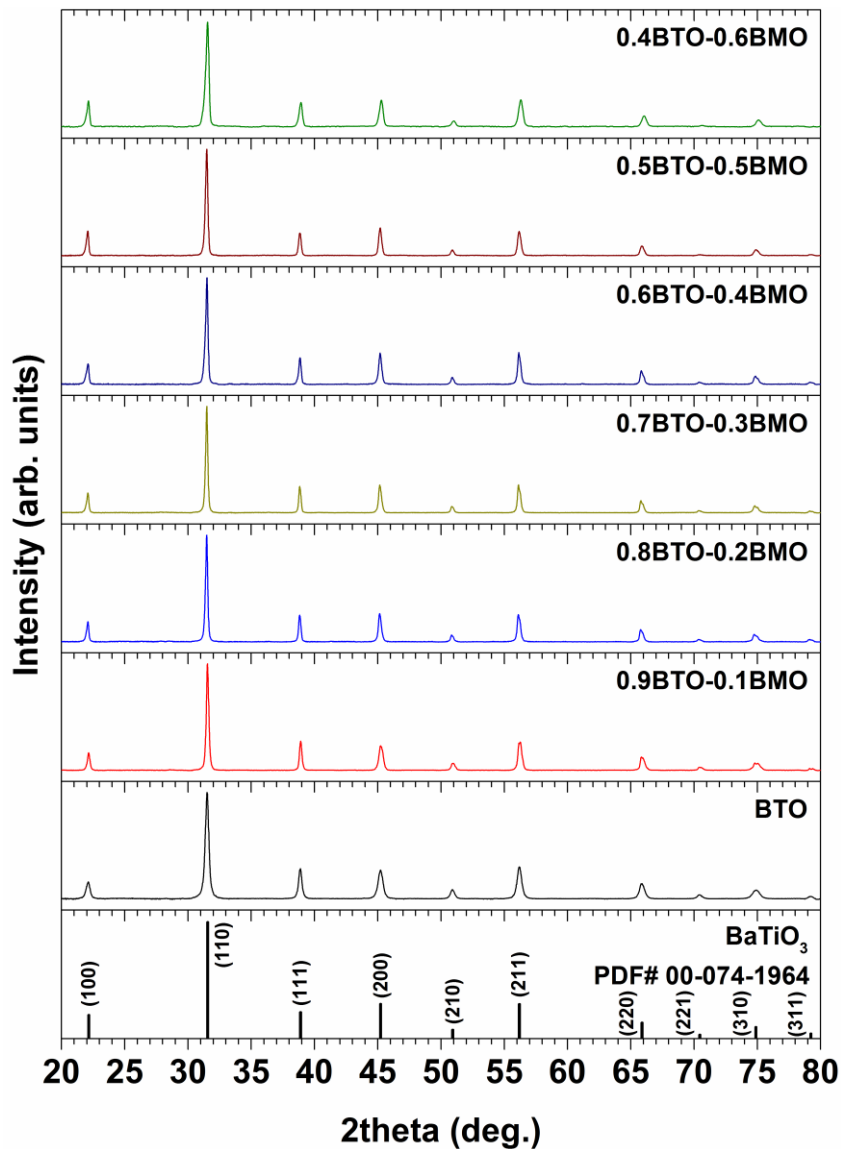
Figure 14. XRD patterns of (1-x)BTO-xBMO solid solutions.

Raman spectroscopy is able to provide detailed information on a short range structure or local symmetry. Figure 15 compares Raman spectra of (1-x)BTO-xBMO solid solutions at different x values. In the case of pristine BTO (x = 0), the strong band at 520 cm^{-1} belongs A_1 and E symmetries of transverse optical (TO) phonon mode [A_1, E (TO)]. The second intense and broad band is located near 260 cm^{-1}; this feature is associated with A_1 (TO) phonon [144–146]. The sharp low intensity band near 305 cm^{-1} is associated with B1 and E symmetries of longitudinal optical (LO) and TO phonon modes [B_1, E (TO + LO)] and high frequency band near 716 cm^{-1} is related with A_1, E (LO) phonons. These bands are characteristic for $BaTiO_3$ ferroelectric phase with tetragonal symmetry [144–146]. Despite the fact that Raman activity is not expected in cubic BTO, the presence of Raman modes in paraelectric polycrystalline BTO with cubic structure was also reported. It was suggested that Raman activity can arise due to several reasons such as displacement of Ti ions resulting in imperfect cubic symmetry, grain boundaries and intergrain stresses [144]. It should be noted that observed bands corresponds to several phonons because frequencies of the modes are very close [144]. Observed bands

26

in our Raman spectrum of studied compound with x = 0 are characteristic for BaTiO$_3$ [144–149]. Introduction of BMO (x = 0.1) into BTO compound results in considerable spectral changes. The new well-defined band appears near 655 cm^{-1}. Based on lattice dynamics calculation this band was assigned to the symmetric stretching B$_{2g}$ mode of MnO$_6$ octahedra [150]. No spectral signatures for secondary phase Bi$_2$O$_3$ compound often visible in BMO was detected [151]; the characteristic Bi$_2$O$_3$ Raman band is located at 610−620 cm^{-1} [152]. The broad feature near 1234 cm^{-1} most likely is related with overtone of B$_{2g}$ mode. Two prominent bands of BTO lattice located at 520 and 260 cm^{-1} downshift to 514 and 242 cm^{-1}, respectively. This indicates distortion of BTO structure induced by BMO. Interestingly, the characteristic spectral marker bands for BaTiO$_3$ ferroelectric phase at 305 and 716 cm^{-1} are still visible in the spectrum of mixed compound indicating preservation of the dominant tetragonal symmetry after introduction of BMO at x = 0.1 level. These bands disappear at higher content of BMO (x ≥ 0.3).
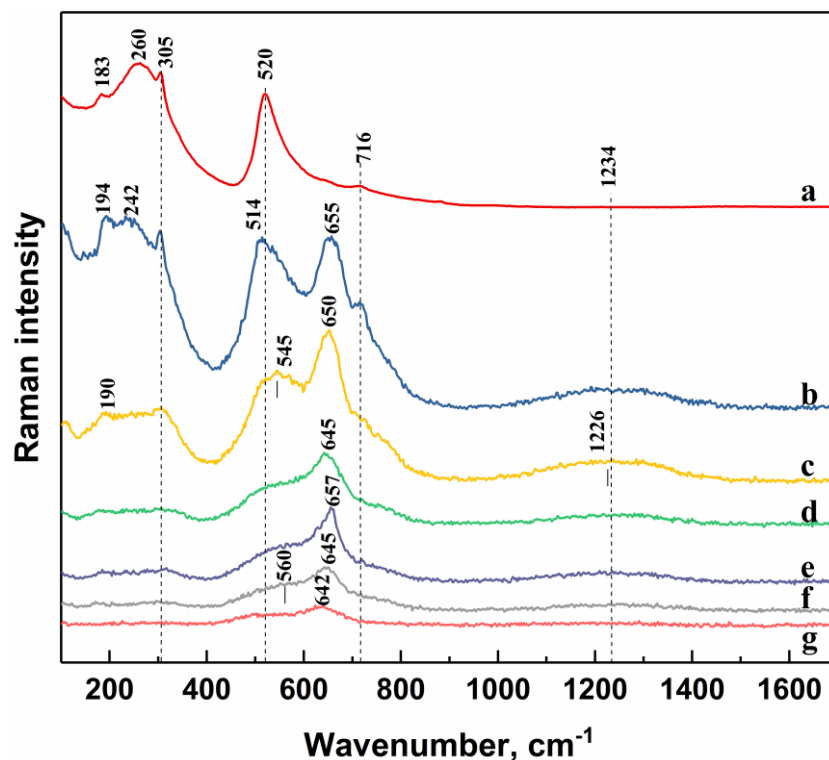

Figure 15. Raman spectra of BTO (a), 0.9BTO-0.1BMO (b), 0.8BTO-0.2BMO (c), 0.7BTO-0.3BMO (d), 0.6BTO-0.4BMO (e), 0.5BTO-0.5BMO (f), 0.4BTO-0.6BMO (g) solid solutions,

SEM was employed to study the influence of chemical composition of the synthesized compounds on their morphological features. SEM images of BTO and representative BTO-BMO solid solutions are shown in Figure 16. It is seen that powders of pristine BTO are composed of mostly uniform nanosized particles, however some larger aggregates are also seen. Size of these particles was found to be nearly 50–100 nm. Partial substitution of BTO by BMO evidently promotes significant growth of the grains. The samples composed of 20 mol% of BMO reveal visibly larger grains, which vary from approximately 150 to 400 nm in size. Further increase in percentage of BMO component to 40 mol% resulted in further growth of the grains to the range of 0.2–1 μm. Finally, the largest grains

were observed for 0.4BTO-0.6BMO solid solution, which were ranged from around 3 to 9 μm and showed approximately 100 fold growth in comparison to pristine BTO. It is known that multicomponent oxide systems can aggregate some impurities in a grain boundary region, which affects the local structure, chemistry and thus governs overall properties of the materials [153]. As seen in Figure 16 no significant amounts of impurities were detected in the grain boundary region, which confirms the formation of solid solution.
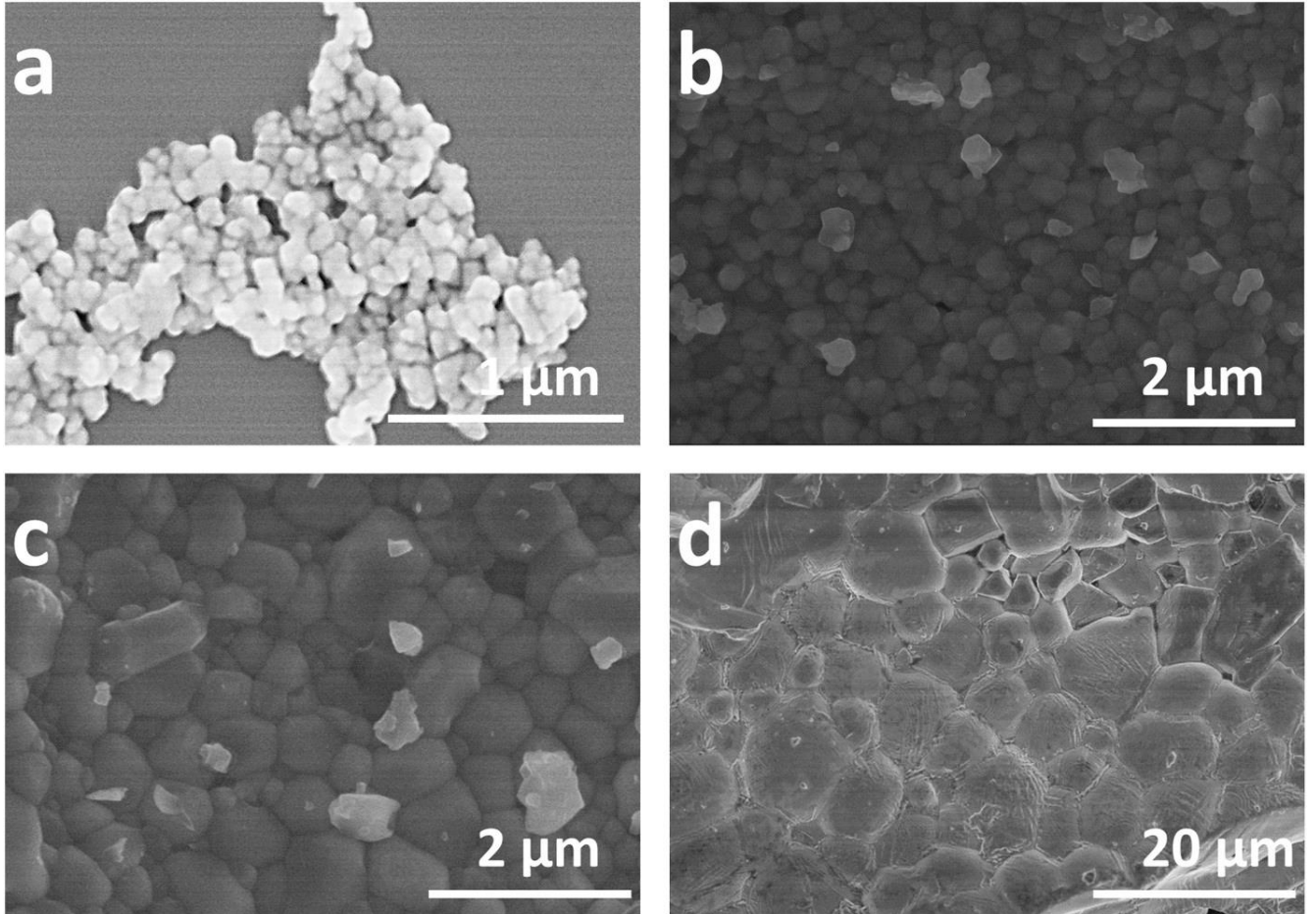
Figure 16. SEM images of $BaTiO_3$ (a), $0.8BaTiO_3$-$0.2BiMnO_3$ (b), $0.6BaTiO_3$-$0.4BiMnO_3$ (c) and $0.4BaTiO_3$-$0.6BiMnO_3$ (d) solid solutions.

Dependence of the magnetization on applied magnetic field strength and chemical composition of solid solutions was further studied. Magnetization curves of all synthesized compounds are depicted in Figure 17. It is evident that magnetization of the samples indicates paramagnetic state of materials. For paramagnets magnetization is proportional to magnetic field M = χH, where volume magnetic susceptibility χ according to Curie-Weis law [154] is:

$$\chi = \frac{C}{T - T_C} = \frac{n}{3k_b} \cdot \frac{\mu_{eff}^2}{T - T_C}$$

(3)

Inclination of curves is defined by effective magnetic moment of atom μ_{eff}, number of paramagnetic atoms per volume n, Curie (magnetic ordering) temperature T_C which depends on composition and structure of the samples. It is seen that for all BMO-containing samples magnetization is proportional to magnetic field strength. Moreover, clear dependence of magnetization values on chemical composition of powders was observed. Magnetization gradually increases as percentage of BMO component in prepared solid solutions increases. It is also known that magnetization of materials can exhibit size-dependent behavior [155,156], however for our materials the change in chemical composition goes hand in hand with an increase of the grain size, therefore it would be baseless to state unequivocally that magnetization of BTO-BMO solid solutions is exclusively composition-dependent.
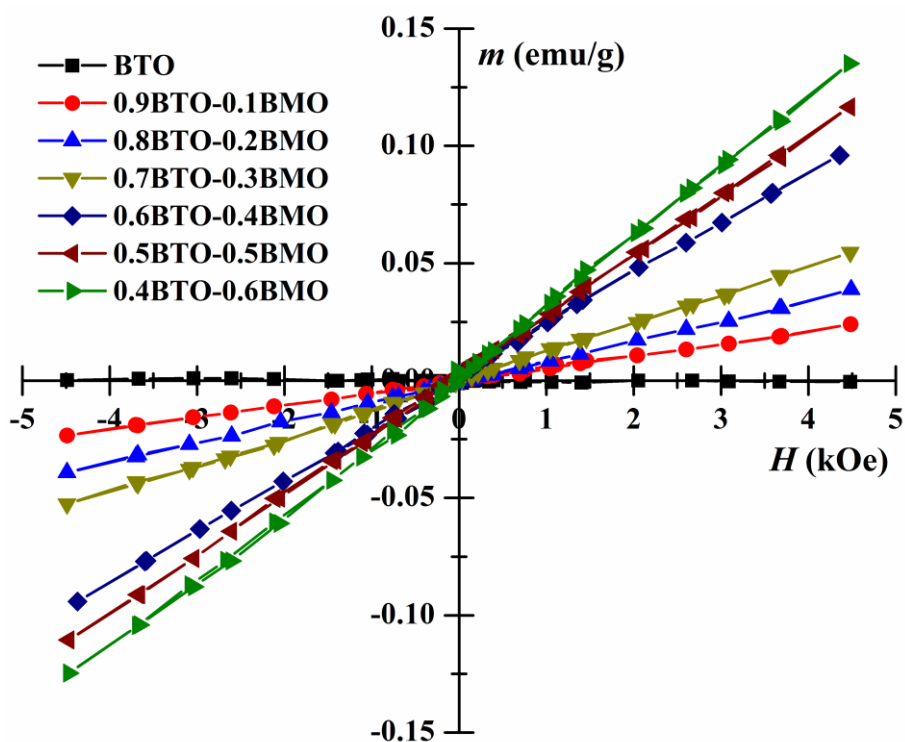

Figure 17. Magnetization curves of BTO-BMO solid solutions.

3.3   SrTiO$_3$–BiMnO$_3$ solid solutions

Thermogravimetric analysis was performed for Sr-Ti-O and Sr-Bi-Ti-Mn precursor gels in order to investigate thermal decomposition behavior. TG/DTG/DSC curves of the gel corresponding to final STO composition are depicted in Figure 18. It can be seen that the Sr-Ti-O gel degradation occurs in 3 main steps. First step can be associated with absorbed water loss and only small amount of initial weight is lost. This process happens at around 100 °C. Next, the second weight loss centered around 300 °C took place, which can be attributed to decomposition of nitrates and organic components. Last weight loss accompanied by a strong exothermic signal happens at 450-500 °C range, which associated with decomposition of residual organic parts of the gel. At above 500 °C residual mass remains constant. Total weight loss calculated from TG curve was 82 %.
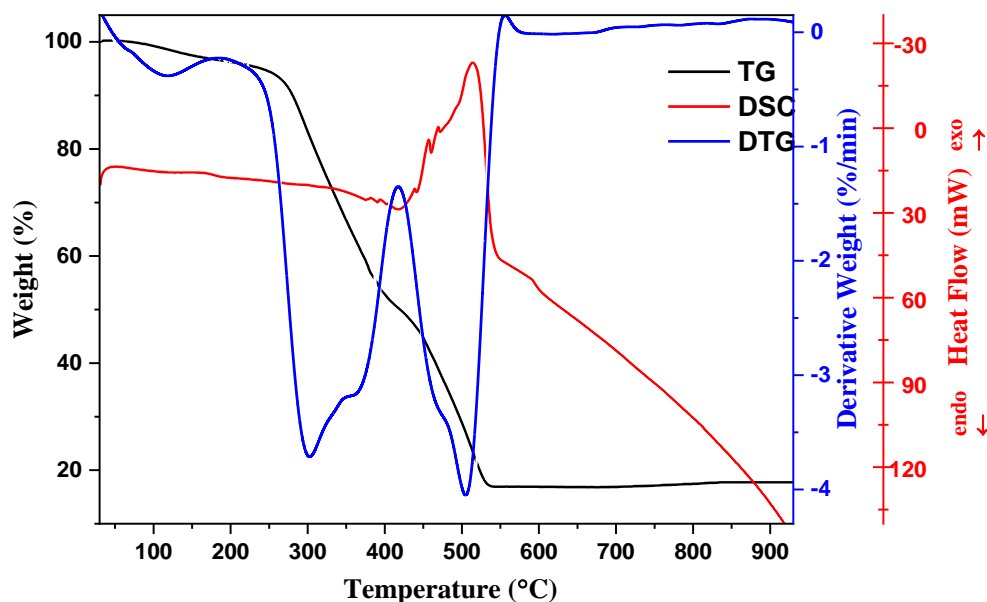
Figure 18. TG/DTG/DSC curves of Sr-Ti-O precursor gel.

For comparison the thermal decomposition of the gel with the highest BMO concentration was studied (Figure 19.) It can be observed that degradation occurs in very similar 3 step way. First and non-significant weight loss occurs at low temperatures and is associated with removal of water. It can be seen that the second step is centered around 260 °C, which is slightly lower than in STO gel case. The last decomposition step followed by strong exothermic signal appears at nearly 450 °C and it also can be related to disintegration of residual organic parts. Above 460 °C residual mass remains constant. 80 % weight loss was calculated from TG curve.
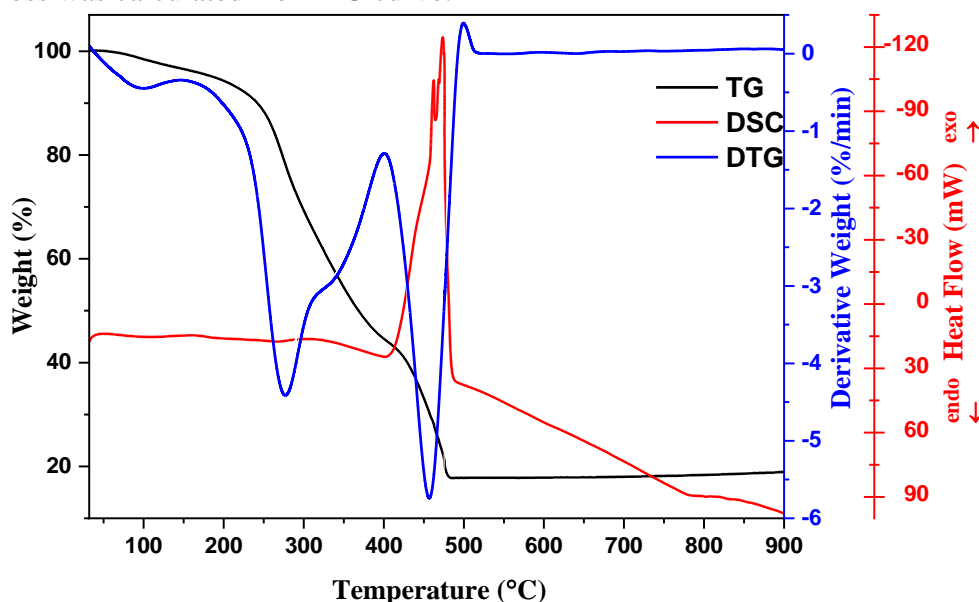

Figure 19. TG/DTG/DSC curves of Sr-Ti-O precursor gel.

For all obtained STO-BMO solid solutions the XRD analysis was done and results are demonstrated in Figure 20. From Figure 20 we can clearly see that in all cases perovskite structure are formed and it matches the $SrTiO_3$ PDF card (PDF# 96-151-2125).
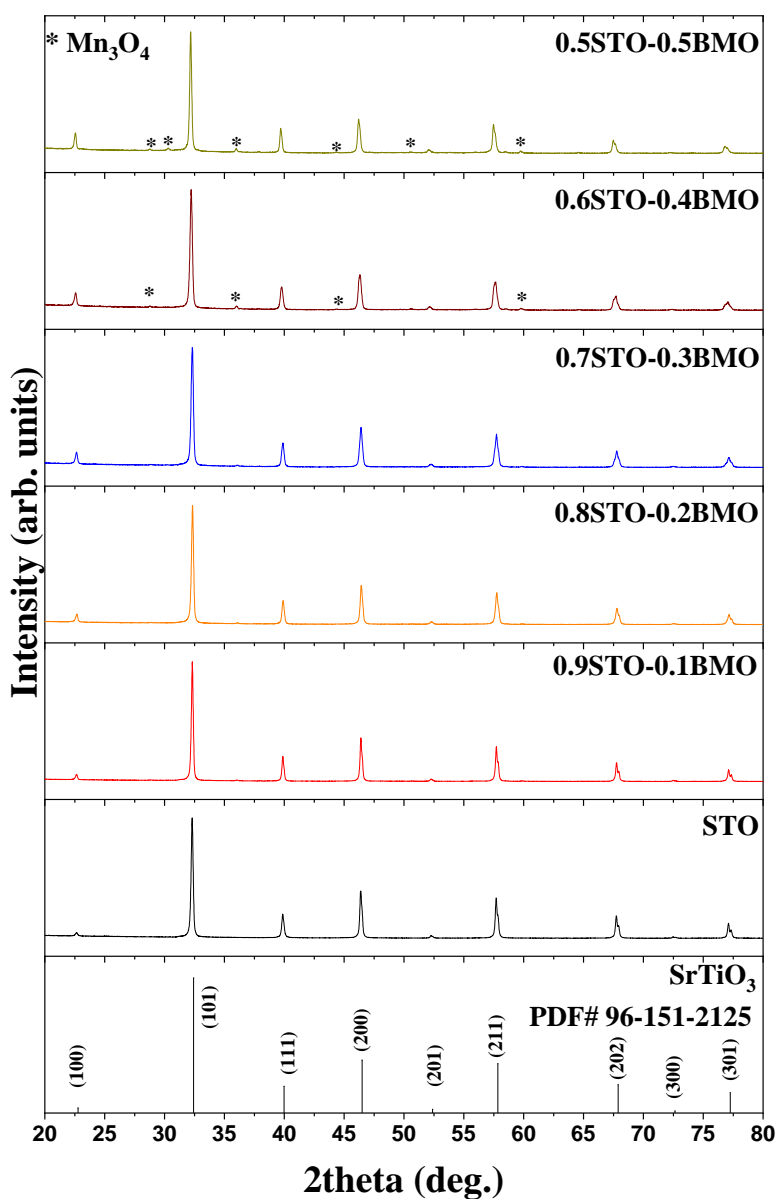
Figure 20. XRD patterns of (1-x)SrTiO$_3$-xBiMnO$_3$ solid solutions (when x varies from 0 to 0.5). *
represents the impurity phase of Mn$_3$O$_4$.

This perovskite structure was cubic with Pm$\bar{3}$m space group. It was observed that most of the samples
are phase pure, without any impurity phases, except for solid solutions with higher BiMnO$_3$
concentration (40-50 %). Mn$_3$O$_4$ (PDF# 96-151-4241) was determined as the secondary phase for
0.6STO-0.4BMO and 0.5STO-0.5BMO compounds. After carrying Rietvield refinement the amount of
Mn$_3$O$_4$ phase was calculated. For 0.5STO-0.5BMO solid solution the amount of neighboring phase was
about 5 % and for 0.6STO-0.4BMO – around 6 %. Introduction of BMO component into STO crystal
lattice does not cause any visible changes in the XRD patterns for solid solutions containing 10-30 %
BMO. No extra peaks or peak splitting were observed for these samples. Moreover, there was no

change in the peak positions in the XRD patterns. Only for 0.6STO-0.4BMO and 0.5STO-0.5BMO solid solutions peak positions are slightly shifted to lower 2Θ angle.

The morphology of the synthesized $(1-x)SrTiO_3-xBiMnO_3$ powders was examined using SEM. SEM images of STO and representative STO-BMO solid solutions are shown in Figure 21. It can be seen that $SrTiO_3$ solids are composed mostly of uniform nanosized particles of 40-100 nm size. Partial substitution of STO by BMO unequivocally promotes significant growth of the grains. Sample with 20 mol% BMO displays visibly larger grains. Grains with approximately 1.1-2 μm size can be seen. Smaller particles with 0.25-0.6 μm can also be viewed in this sample. Further increase in percentage of BMO component to 40 mol% resulted in further growth of the grains to the range of 1.2–3 μm. Finally, the largest grains were observed for 0.5STO-0.5BMO sample, which ranged from 1.4–5 μm. It is known that multicomponent oxide systems can aggregate some impurities in a grain boundary region, but nothing was detected in the grain boundary region for these samples.
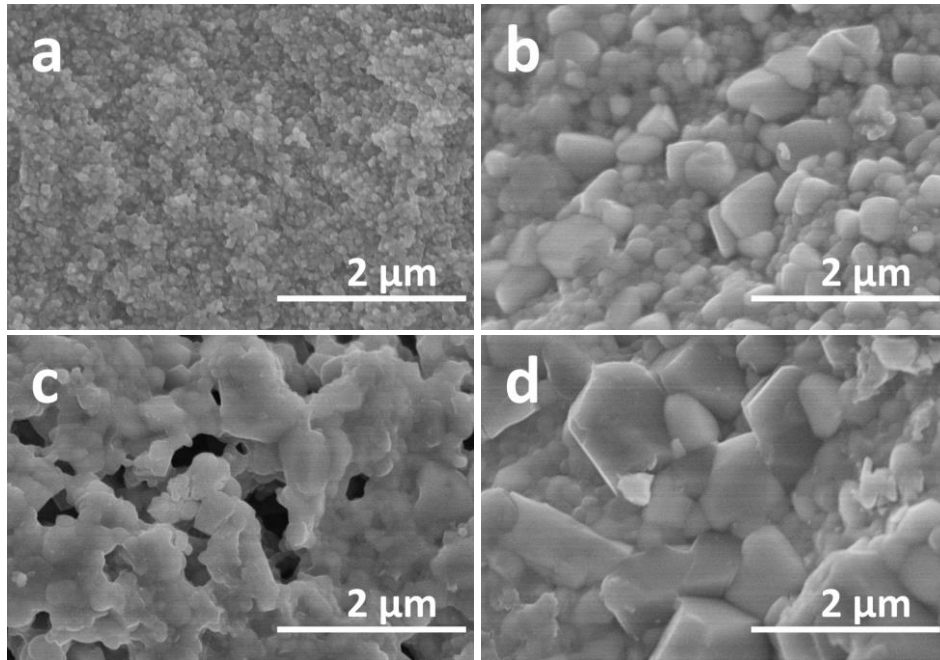

Figure 21. SEM images of $SrTiO_3$ (a), $0.8SrTiO_3-0.2BiMnO_3$ (b), $0.6SrTiO_3-0.4BiMnO_3$ (c) and $0.5SrTiO_3-0.5BiMnO_3$ (d) solid solutions.

CONCLUSIONS

1. For the first time $Bi_xLa_{1-x}MnO_{3+\delta}$ solid solutions (in the range of x = 0.0–0.65) have been prepared by simple, rapid, and environmentally friendly sol–gel combustion method which does not require an addition of external solvent. The results of XRD analysis showed that synthesized $Bi_xLa_{1-x}MnO_{3+\delta}$ powders with x = 0.0–0.3 showed trigonal crystal structure with space group $R\bar{3}c$. With increasing amount of $BiMnO_3$, the transformation of crystal cell to cubic Pm3m space group took place. Moreover, grain size increased significantly with an increase of $BiMnO_3$ amount in solid solutions.

2. The magnetization measurements demonstrated that all $Bi_xLa_{1-x}MnO_{3+\delta}$ samples were paramagnetic and no saturation of magnetization at applied magnetic fields was observed. The structural changes from trigonal to cubic cell resulted in decrease of magnetization. Maximal percentage of $BiMnO_3$ component was determined to be 0.65 mol%.

3. The bulk $(1-x)BaTiO_3-xBiMnO_3$ solid solutions have been synthesized for the first time employing an aqueous sol-gel method. It was demonstrated that single-phase compounds can be obtained in the compositional range from 0 to 60 mol% of $BiMnO_3$. The perovskite crystal structure was determined for all synthesized compounds regardless of chemical composition. Substitution of $BaTiO_3$ by $BiMnO_3$ lead to the drastic growth of the grains.

4. Magnetization measurements showed that all $BiMnO_3$-containing samples could be characterized by paramagnetic behavior. Clear correlation between magnetization values and composition of the materials was observed, magnetization values increased with increase of $BiMnO_3$ content in the solid solutions.

5. Aqueous sol-gel method was applied for the preparation of $(1-x)SrTiO_3-xBiMnO_3$ solid solutions. XRD data for $(1-x)SrTiO_3-xBiMnO_3$ samples revealed that at higher $BiMnO_3$ concentration (x = 40-50%) the Mn_3O_4 impurities have formed. Other solid solutions had cubic crystal structure with $Pm\bar{3}m$ space group. Substitution of $SrTiO_3$ by $BiMnO_3$ resulted in significant growth of the grains similarly as in the case of $(1-x)BaTiO_3-xBiMnO_3$.

SANTRAUKA

VILNIAUS UNIVERSITETAS
CHEMIJOS IR GEOMOKSLŲ FAKULTETAS

DOVYDAS KAROBLIS
BiMnO3 turinčių kietųjų tirpalų sintezė ir tyrimas

Šiame darbe buvo susintetinti įvairūs perovskito struktūrą turintys $BiMnO_3$ kietieji tirpalai. Zolių–gelių degimo metodas buvo pirmą kartą pritaikytas $Bi_xLa_{1-x}MnO_{3+\delta}$ kietųjų tirpalų sintezei. XRD analizės duomenys parodė, jog didžiausias galimas $BiMnO_3$ komponento kiekis $LaMnO_3$ sistemoje yra 65 mol%. Kintant $Bi_xLa_{1-x}MnO_{3+\delta}$ kietųjų tirpalų sudėčiai, buvo pastebėti pasikeitimai ir perovskito struktūroje, kuri pakito iš trigoninės (kai x=0,1-0,3) į kubinę (x=0,4-0,65). Nustatyta, jog visi gauti junginiai kambario temperatūroje yra paramagnetiniai, o įmangnetėjimo dydis priklauso nuo struktūros bei cheminės sudėties. Zolių-gelių metodas buvo taip pat panaudotas $(1-x)BaTiO_3-xBiMnO_3$ ir $(1-x)SrTiO_3-xBiMnO_3$ kietųjų tirpalų sintezei. XRD analizė parodė, jog visų junginių kristalinė struktūra yra kubinė. Didinant $BiMnO_3$ kiekį abejose junginių serijose, perovskito struktūra nepakito. Didžiausias $BiMnO_3$ kiekis $(1-x)BaTiO_3-xBiMnO_3$ serijoje yra 60 %, o $(1-x)SrTiO_3-xBiMnO_3$ – 50 %. Tačiau $(1-x)SrTiO_3-xBiMnO_3$ serijos junginiuose, kur x=0,4-0,5, susidaro pašalinė Mn_3O_4 fazė. $(1-x)BaTiO_3-xBiMnO_3$ serijos junginių magnetiniai matavimai atskleidė, jog kambario temperatūroje visi jie yra paramagnetiniai. SEM analizės rezultatai parodė, jog įvedant į $BaTiO_3$ bei $SrTiO_3$ struktūras didesnį $BiMnO_3$ kiekį, suintensyvėjo atitinkamų medžiagų grūdelių augimas.

SUMMARY

VILNIUS UNIVERSITY
FACULTY OF CHEMISTRY AND GEOSCIENCES

DOVYDAS KAROBLIS
Synthesis and characterization of
BiMnO$_3$ containing solid solutions

Perovskite-type compounds containing BiMnO$_3$ were synthesized in this work. For the first time sol-gel combustion method was succesfully employed for the preparation of Bi$_x$La$_{1-x}$MnO$_{3+\delta}$ solid solutions. XRD analysis demonstrated that the maximal amount of BiMnO$_3$ in LaMnO$_3$ structure was 65 mol%. The phase transition was observed from trigonal (when x=0.1-0.3) to cubic (when x=0.4-0.65). All Bi$_x$La$_{1-x}$MnO$_{3+\delta}$ samples demonstrated paramagnetic behavior at room temperature and magnetization depends on chemical structure and composition. Sol-gel method was applied for preparation of (1-x)BaTiO$_3$-xBiMnO$_3$ and (1-x)SrTiO$_3$-xBiMnO$_3$ solid solutions. Cubic structure was observed for all samples. Increase in BiMnO$_3$ amount did not cause any visible changes in perovskite structure. Maximal amount of BiMnO$_3$ in (1-x)BaTiO$_3$-xBiMnO$_3$ solid solutions was 60 % and for (1-x)SrTiO$_3$-xBiMnO$_3$ – 50 %. Secondary Mn$_3$O$_4$ phase was observed for (1-x)SrTiO$_3$-xBiMnO$_3$ (where x=0.4-0.5). Magnetic measurements of (1-x)BaTiO$_3$-xBiMnO$_3$ system demonstrated that at room temperature all samples are paramagnetic. SEM analys showed, that increase in BiMnO$_3$ amount resulted in significant growth of the grains.

PUBLICATIONS

List of articles:

1. Karoblis, Dovydas, Mazeika, Kestutis, Baltrunas, Dalis Antanas, Lukowiak, Anna, Strek, Wieslaw, Zarkov, Aleksej, & Kareiva, Aivaras. (2020). Novel synthetic approach to the preparation of single-phase $BixLa1-xMnO3\ \delta$ solid solutions. Journal of Sol-gel Science and Technology, 93, 650-656.

2. Karoblis, Dovydas, Zarkov, Aleksej, Mazeika, Kestutis, Baltrunas, Dalis Antanas, Niaura, Gediminas, Beganskiene, Aldona, Kareiva, Aivaras. (2020). Sol-gel synthesis, structural, morphological and magnetic properties of $BaTiO3–BiMnO3$ solid solutions, Ceramics International. Accepted for publication. doi.org/10.1016/j.ceramint.2020.03.209

List of conferences:

1. Zarkov, Aleksej, Karoblis, Dovydas, Popov, Anton, Kareiva, Aivaras. (2018). On the synthesis and characterization of perovskite manganites by sol-gel combustion synthesis route. Advanced Materials and Technologies 2018 : Book of Abstracts of 20th International Conference-school, 27-31 August 2018, Palanga, Lithuania, 76.

2. Karoblis, Dovydas, Zarkov, Aleksej, Kareiva, Aivaras. (2019). Lanthanum substituted $BiMnO3$ synthesis and characterization. Open Readings 2019 : 62nd International Conference for Students of Physics and Natural Sciences, March 19-22, 2019, Vilnius, Lithuania : Abstract Book, 100.

3. Karoblis, Dovydas, Zarkov, Aleksej, Kareiva, Aivaras. (2019). Synthesis of (1-x)$BaTiO3·xBiMnO3$ solid solutions via sol-gel method. Chemistry and Chemical Technology: Lithuanian Chemists Conference, 2019 May 16, Lithuanian Academy of Sciences, Vilnius: Conference Book, 72.

ACKNOWLEDGEMENTS

REFERENCES

1. M. T. Sebastian, *Dielectric materials for wireless communication*, Elsevier (2010).
2. C. J. Bartel *et al.*, *Sci. Adv.* 5, (2019).
3. M. Johnsson, P. Lemmens, Crystallography and Chemistry of Perovskites. *Handb. Magn. Adv. Magn. Mater.* (2007).
4. T. Zheng, J. Wu, D. Xiao, J. Zhu, *Prog. Mater. Sci.* 98, 552–624 (2018).
5. D. D. L. Chung, *Carbon composites: Composites with carbon fibers, nanofibers, and nanotubes: Second edition* (2016).
6. L. Da Conceião, A. M. Silva, N. F. P. Ribeiro, M. M. V. M. Souza, *Mater. Res. Bull.* 46, 308–314 (2011).
7. M. Ghasdi, H. Alamdari, *Sensors Actuators B Chem.* 148, 478–485 (2010).
8. J. W. Fergus, *Sensors Actuators B Chem.* 123, 1169–1179 (2007).
9. N. Bonanos, K. S. Knight, B. Ellis, *Solid State Ionics*. 79, 161–170 (1995).
10. F. Wang, D. Chen, Z. Shao, *J. Power Sources*. 216, 208–215 (2012).
11. M. Bowen *et al.*, *Appl. Phys. Lett.* 82, 233–235 (2003).
12. A. F. Moreira Dos Santos *et al.*, (2004).
13. E. Montanari *et al.*, *Chem. Mater.* 17, 1765–1773 (2005).
14. S. T. Norberg, S. Hull, R. Mathieu, S. G. Eriksson, *Chem. Commun.* 46, 1455–1457 (2010).
15. J. Wang, *Multiferroic Materials: Properties, Techniques, and Applications*, CRC Press, (2016).
16. F. D. Morrison, D. C. Sinclair, A. R. West, *Int. J. Inorg. Mater.* 3, 1205–1210 (2001).
17. R. Li, C. Zhang, J. Liu, J. Zhou, L. Xu, *Mater. Res. Express*. 6, 102006 (2019).
18. M. Johnsson, P. Lemmens, *Handb. Magn. Adv. Magn. Mater.* 4, 1–9 (2007).
19. F. S. GALASSO, in *International Series of Monographs in Solid State Physics*, F. S. B. T.-S. pp. 3–49 (1969).
20. S. Uma, A. R. Raju, J. Gopalakrishnan, *J. Mater. Chem.* 3, 709–713 (1993).
21. P. P. Khirade, thesis, Dr. Babasaheb Ambedkar Marathwada University (2017).
22. T. Ishihara, T. Properties, *Springer Handb. Electron. Photonic Mater.*, 1405–1420 (2017).
23. K. Bergum *et al.*, *Dalt. Trans.* 40, 7583–7589 (2011).
24. H. Dong, Z. Wu, F. Wu, J. Li, *Phys. Status Solidi - Rapid Res. Lett.* 12, 1–5 (2018).
25. A. A. Belik *et al.*, *Chem. Mater.* 18, 133–139 (2006).
26. S. Stølen, E. Bakken, C. E. Mohn, *Phys. Chem. Chem. Phys.* 8, 429–447 (2006).
27. V. M. Goldschmidt, *Naturwissenschaften*. 14, 477–485 (1926).
28. X. Liu, R. Hong, C. Tian, *J. Mater. Sci. Mater. Electron.* 20, 323 (2008).
29. C. Li, K. C. K. Soh, P. Wu, *J. Alloys Compd.* 372, 40–48 (2004).
30. F. Thaler, M. Müller, R. Spatschek, *AIMS Mater. Sci.* 3, 1126–1137 (2016).
31. K. J. Choi *et al.*, *Science (80)* (2019).
32. F. P. Sun, Z. Chaudhry, C. Liang, C. A. Rogers, *J. Intell. Mater. Syst. Struct.* 6, 134–139 (1995).
33. N. F. Atta, A. Galal, E. H. El-Ads, *Perovskite Mater. - Synth. Characterisation, Prop. Appl.* (2016).
34. I. S. Zheludev, *Physics of Crystalline Dielectrics* (1995).
35. J. Phillips, *Mater. (Basel, Switzerland)*. 11, 1519 (2018).
36. J. Ilic, K. H. J. Buschow et al., Eds. Elsevier, Oxford pp. 9629-9633 (2001).
37. T. Tanaka, G. C. Montanari, R. Mulhaupt, *IEEE Trans. Dielectr. Electr. Insul.* 11, 763–784 (2004).
38. J. H. Park *et al.*, *J. Korean Phys. Soc.* 49, 680–683 (2006).
39. N. F. Muhamad, R. A. Maulat Osman, M. S. Idris, M. N. Mohd Yasin, *EPJ Web Conf.* 162, 2–5 (2017).

40. I. P. Raevski, S. A. Prosandeev, A. S. Bogatin, M. A. Malitskaya, L. Jastrabik, *J. Appl. Phys.* 93, 4130–4136 (2003).
41. A. Gjelsvik, *J. Biomech.* (1973).
42. J. Tichý *et al.*, in *Fundamentals of Piezoelectric Sensorics* (2010).
43. Y. Xu, *Ferroelectric materials and their applications*, Elsevier (2013).
44. I. Chilibon, J. N. Marat-Mendes, *J. Sol-Gel Sci. Technol.* 64, 571–611 (2012).
45. N. A. Spaldin, *Top. Appl. Phys.* 105, 175–218 (2007).
46. M. Lallart, *Ferroelectrics: characterization and modeling* (BoD–Books on Demand, 2011).
47. W. D. Callister Jr, D. G. Rethwisch, *Fundamentals of materials science and engineering: an integrated approach* (John Wiley & Sons, 2012).
48. C. B. Carter, M. G. Norton, *Ceramic materials: science and engineering* (Springer, 2007), vol. 716.
49. E. Pereloma, D. V Edmonds, *Phase transformations in steels: fundamentals and diffusion-controlled transformations*, Elsevier (2012).
50. G. Rangarajan, *Materials science*, Tata McGraw-Hill Education, (2004).
51. S. Zhang, D. Zhao, *Advances in magnetic materials: processing, properties, and performance* (CRC press, 2017).
52. A. D. of O. T. C. Library, *Minerals* (Cambridge University Press, 1975).
53. M. B. T.-F. of M. Reis, Ed., Academic Press, Boston (2013).
54. Y. Tomioka, Y. Tokura, Colossal Magnetoresistive Oxides (2000).
55. T. Kimura *et al.*, *Nature*. 426, 55–58 (2003).
56. J. Kanamori, *J. Appl. Phys.* 31, S14–S23 (1960).
57. M. Zlatar, C. W. Schläpfer, E. P. Fowe, C. Daul, *Pure Appl. Chem.* 81, 1397–1411 (2009).
58. J. A. Alonso, M. J. Martínez-Lope, M. T. Casais, M. T. Fernández-Díaz, *Inorg. Chem.* 39, 917–923 (2000).
59. N. V Kasper, I. O. Troyanchuk, *J. Phys. Chem. Solids*. 57, 1601–1607 (1996).
60. M. Tachibana, T. Shimoyama, H. Kawaji, T. Atake, E. Takayama-Muromachi, *Phys. Rev. B - Condens. Matter Mater. Phys.* 75, 2–6 (2007).
61. M. Kenzelmann *et al.*, *Phys. Rev. Lett.* 95, 87206 (2005).
62. T. Arima *et al.*, *Phys. Rev. Lett.* 96, 97202 (2006).
63. J.-S. Zhou, J. B. Goodenough, *Phys. Rev. Lett.* 94, 65501 (2005).
64. K. K. ASISH, *MAGNETIC PEROVSKITES: Synthesis, Structure and Physical Properties* , SPRINGER, (2017).
65. J. Jin *et al.*, *Adv. Funct. Mater.* 24, 1067–1073 (2014).
66. G. Schileo *et al.*, *J. Am. Ceram. Soc.* 99, 1609–1614 (2016).
67. M. Fiebig, T. Lottermoser, D. Meier, M. Trassin, *Nat. Rev. Mater.* 1, 16046 (2016).
68. R. M. Thankachan, R. Balakrishnan, *Synthesis Strategies of Single-Phase and Composite Multiferroic Nanostructures*, Elsevier Ltd., (2018).
69. R. P. Ummer *et al.*, *RSC Adv.* 5, 67157–67164 (2015).
70. S. Narendra Babu, J.-H. Hsu, Y. S. Chen, J. G. Lin, *J. Appl. Phys.* 109, 07D904 (2011).
71. Y.-H. Chu *et al.*, *Nat. Mater.* 7, 478–482 (2008).
72. T. Zhao *et al.*, *Nat. Mater.* 5, 823–829 (2006).
73. S. Y. Park *et al.*, *InfoMat*. 1, 289–316 (2019).
74. M. C. Williams, D. Shekhawat, J. J. Spivey, D. A. B. T.-F. C. T. for F. P. Berry, Eds. Elsevier, Amsterdam, pp. 11–27 (2011).
75. A. Coralli *et al.*, P. E. V. B. T.-S. and E. of H.-B. E. T. de Miranda, Ed. Academic Press, pp.39–122 (2019).
76. S. J. Skinner, *Int. J. Inorg. Mater.* 3, 113–121 (2001).

77.	Z. Shao, S. Haile, *Nature*. 431, 170–173 (2004).

78.	N. Bao, A. Gupta, *Encycl. Inorg. Bioinorg. Chem.*, 1–15 (2011).

79.	J. T. Heron *et al.*, *Nature*. 516, 370–373 (2014).

80.	S. P. Jiang *et al.*, *J. Power Sources*. 176, 82–89 (2008).

81.	J. A. Alonso *et al.*, *J. Mater. Chem.* 7, 2139–2144 (1997).

82.	J. Töpfer, J. B. Goodenough, *J. Solid State Chem.* 130, 117–128 (1997).

83.	M. Dine El Hannani *et al.*, *Mater. Sci. Semicond. Process.* 11, 81–86 (2008).

84.	S. A. Hosseini *et al.*, *J. Sol-Gel Sci. Technol.* 85, 647–656 (2018).

85.	M. M. Vopson, *Crit. Rev. Solid State Mater. Sci.* 40, 223–250 (2015).

86.	A. A. Belik *et al.*, *J. Am. Chem. Soc.* 129, 971–977 (2007).

87.	D. P. Kozlenko *et al.*, *J. Alloys Compd.* 585, 741–747 (2014).

88.	A. A. Belik *et al.*, *J. Am. Chem. Soc.* 132, 8137–8144 (2010).

89.	W. Prellier, M. P. Singh, P. Murugavel, *J. Phys. Condens. Matter*. 17, R803 (2005).

90.	F. Sugawara, Y. Syono, S. Akimoto, *J. Phys. Soc. Japan*. 20, 1529 (1965).

91.	B. W. Lee, P. S. Yoo, V. B. Nam, K. R. N. Toreh, C. U. Jung, *Nanoscale Res. Lett.* 10, 47 (2015).

92.	F. El-Mellouhi, E. N. Brothers, M. J. Lucero, I. W. Bulik, G. E. Scuseria, *Phys. Rev. B - Condens. Matter Mater. Phys.* 87, 1–11 (2013).

93.	H. Unoki, T. Sakudo, *J. Phys. Soc. Japan*. 23, 546–552 (1967).

94.	A. Heidemann, H. Wettengel, *Zeitschrift für Phys. A Hadron. Nucl.* 258, 429–438 (1973).

95.	A. E. Souza *et al.*, *Cryst. Growth Des.* 12, 5671–5679 (2012).

96.	J. E. Ramos-Sanchez, R. Camposeco, S.-W. Lee, V. Rodríguez-González, *Catal. Today*. 341, 112–119 (2020).

97.	M. E. Lines, A. M. Glass, *Principles and applications of ferroelectrics and related materials* , Oxford university press (2001).

98.	F. Jona, G. Shirane, F. Crystals, *Inc., New York* (1993).

99.	M. Acosta *et al.*, *Appl. Phys. Rev.* 4 (2017).

100.	V. Mishra *et al.*, *J. Appl. Phys.* 122 (2017).

101.	A. J. Moulson, J. M. Herbert, *Electroceramics: materials, properties, applications*, John Wiley & Sons (2003).

102.	L. Wu *et al.*, *Ceram. Int.* 35, 957–960 (2009).

103.	B. G. Rao, D. Mukherjee, B. M. Reddy, *Nanostructures for novel therapy novel approaches for preparation of nanoparticles*, Elsevier Inc., (2017).

104.	D. Wang, G. P. Bierwagen, *Prog. Org. coatings*. 64, 327–338 (2009).

105.	B. G. Rao, D. Mukherjee, B. M. Reddy, in *Micro and Nano Technologies*, D. Ficai, A. M. B. T.-N. for N. T. Grumezescu, Eds., Elsevier, pp. 1–36 (2017).

106.	S. Čižauskaitė *et al.*, *Chemija*. 17 (2006).

107.	H. E. Figen, N. O. Guldal, S. Z. Baykara, *Acta Phys. Pol. A*. 125, 278–280 (2014).

108.	M. Airimioaei *et al.*, *J. Alloys Compd.* 509, 8065–8072 (2011).

109.	A. C. F. M. Costa, M. R. Morelli, R. H. G. A. Kiminami, *J. Mater. Synth. Process.* 9, 347–352 (2001).

110.	R. K. Selvan, C. O. Augustin, L. J. Berchmans, R. Saraswathi, *Mater. Res. Bull.* 38, 41–54 (2003).

111.	A. Sutka, G. Mezinskis, *Front. Mater. Sci.* 6, 128–141 (2012).

112.	R. V Mangalaraja, S. Ananthakmar, M. P, F. D. Gnanam, M. Awano, *Mater. Sci. Eng. A*. 367, 301–305 (2004).

113.	A. S. Mukasyan, P. Epstein, P. Dinka, *Proc. Combust. Inst.* 31, 1789–1795 (2007).

114.	A. Zarkov, L. Mikoliunaite, A. Katelnikovas, S. Tautkus, A. Kareiva, *Chem. Pap.* 72, 129–138

(2018).

115. L. Kopanja, I. Milosevic, M. Panjan, V. Damnjanovic, M. Tadic, *Appl. Surf. Sci.* 362, 380–386 (2016).
116. M. Tadić, D. Marković, M. Panjan, V. Spasojević, *Ceram. Int.* 42, 19365–19371 (2016).
117. H. Schmalzried, N. B. Hannay, Ed. Springer US, Boston, MA, pp. 233–279 (1976).
118. R. Xu, Y. Xu, *Modern inorganic synthetic chemistry*, Elsevier (2010).
119. A. R. West, *Solid state chemistry and its applications*, John Wiley & Sons (2014).
120. S. Ivanov, *Multiferroic complex metal oxides: Main features of preparation, structure, and properties,* Elsevier Inc., vol. 2. (2012).
121. B. Pongtippitak, S. Thountom, *Ferroelectrics*. 519, 100–105 (2017).
122. A. A. Belik, T. Yokosawa, K. Kimoto, Y. Matsui, E. Takayama-Muromachi, *Chem. Mater.* 19, 1679–1689 (2007).
123. R. Liu *et al.*, *Front. Chem. China*. 1, 398–401 (2006).
124. K. Byrappa, M. Yoshimura, K. Byrappa, M. B. T.-H. of H. T. Yoshimura, Eds. William Andrew Publishing, Norwich, NY, pp. 1–52 (2001).
125. G. Tian, S. Sun, *Cryst. Res. Technol.* 45, 188–194 (2010).
126. S. Wang *et al.*, *Supercritical Water Processing Technologies for Environment, Energy and Nanomaterial Applications*, Springer Nature, (2019).
127. M. Yoshimura, K. Byrappa, *J. Mater. Sci.* 43, 2085–2103 (2007).
128. C. Y. Song, J. Xu, A. Yimamu, L. Wang, *Integr. Ferroelectr.* 153, 33–41 (2014).
129. T. Chen *et al.*, *CrystEngComm*. 21, 4763–4770 (2019).
130. Y. Mao, S. Banerjee, S. S. Wong, *Chem. Commun.* 9, 408–409 (2003).
131. X. Sun *et al.*, *Surf. Coatings Technol.* 320, 527–530 (2017).
132. S. R. Jain, K. C. Adiga, V. R. Pai Verneker, *Combust. Flame*. 40, 71–79 (1981).
133. D. P. Joseph, J. W. Lin, N. P. Kumar, W. C. Chen, J. G. Lin, *J. Magn. Magn. Mater.* 418, 68–75 (2016).
134. I. O. Troyanchuk, O. S. Mantytskaja, H. Szymczak, M. Y. Shvedun, *Low Temp. Phys.* 28, 569–573 (2002).
135. Y. D. Zhao, J. Park, R.-J. Jung, H.-J. Noh, S.-J. Oh, *J. Magn. Magn. Mater.* 280, 404–411 (2004).
136. M. Iqbal, M. N. Khan, A. A. Khan, *J. Magn. Magn. Mater.* 465, 670–677 (2018).
137. A. Barnabé, M. Gaudon, C. Bernard, C. Laberty, B. Durand, *Mater. Res. Bull.* 39, 725–735 (2004).
138. R. D. Shannon, *Acta Crystallogr. Sect. A*. 32, 751–767 (1976).
139. K. Nakamoto, Infrared and Raman Spectra of Inorganic and Coordination Compounds. *Handb. Vib. Spectrosc.* (2001).
140. L. Kebin, L. Xijun, Z. Kaigui, Z. Jingsheng, Z. Yuheng, *J. Appl. Phys.* 81, 6943–6947 (1997).
141. K. Sugawara *et al.*, *AIChE J.* 43, 2837–2843 (1997).
142. Z. Wang *et al.*, *J. Mater. Chem. C*. 1, 522–530 (2013).
143. E. Ciftci, M. N. Rahaman, M. Shumsky, *J. Mater. Sci.* 36, 4875–4882 (2001).
144. U. D. Venkateswaran, V. M. Naik, R. Naik, *Phys. Rev. B*. 58, 14256 (1998).
145. J. Pokorný *et al.*, *J. Appl. Phys.* 109, 114110 (2011).
146. L. Huang *et al.*, *J. Appl. Phys.* 100, 34316 (2006).
147. K. C. Verma, V. Gupta, J. Kaur, R. K. Kotnala, *J. Alloys Compd.* 578, 5–11 (2013).
148. I. J. Clark, T. Takeuchi, N. Ohtori, D. C. Sinclair, *J. Mater. Chem.* 9, 83–91 (1999).
149. S. W. Lu, B. I. Lee, Z. L. Wang, W. D. Samuels, *J. Cryst. Growth*. 219, 269–276 (2000).
150. D. P. Kozlenko *et al.*, *J. Alloys Compd.* 585, 741–747 (2014).
151. P. Toulemonde, P. Bordet, P. Bouvier, J. Kreisel, *Phys. Rev. B*. 89, 224107 (2014).

152. L. Meng, W. Xu, Q. Zhang, T. Yang, S. Shi, *Appl. Surf. Sci.* 472, 165–171 (2019).
153. B. Feng *et al.*, *Nat. Commun.* 7, 1–6 (2016).
154. C. Kittel, P. McEuen, P. McEuen, *Introduction to solid state physics*, Wiley New York, vol. 8. (1996).
155. X. He, W. Zhong, C.-T. Au, Y. Du, *Nanoscale Res. Lett.* 8, 446 (2013).
156. Q. Li *et al.*, *Sci. Rep.* 7, 1–7 (2017).